# JOURNAL OF AEROSPACE SOCIETY MALAYSIA

Volume 1, Issue 1

APRIL 2023

AEROSPACE SOCIETY MALAYSIA
PERSATUAN AEROANGKASA MALAYSIA
Registration No. PPM-001-10-09012017

Toward Greater Heights

JOURNAL OF
AEROSPACE SOCIETY MALAYSIA

**VOLUME 1, ISSUE 1**
**April 2023**

eISSN 3009-0520

B-31-09, Kompleks EVO, Jalan Pusat Bandar 2, Seksyen 9,
43650 Bandar Baru Bangi, Selangor, Malaysia

Email: aeros_journal@aerosmalaysia.my

Tel.: 03-97696394 (Editor-in-Chief)

**Journal of Aerospace Society Malaysia (AEROS Journal)** is an open-access online journal that publishes high-quality research articles in all areas of aeronautics, astronautics and aviation. All submitted articles will undergo peer-review process before they are accepted for publication.

**Publication Frequency:** 3 times a year (end of April, August and December)

# EDITORIAL

## EDITOR-IN-CHIEF

## EDITORS

## LIST OF REVIEWERS FOR THIS ISSUE

# TABLE OF CONTENTS

JOURNAL OF AEROSPACE SOCIETY MALAYSIA

# EXPERIMENTAL VERIFICATION OF A SNUBBING GRIPPER DESIGN FOR FINE WIRE SPECIMENS IN TENSILE TESTING

**Sivasanghari Karunakaran [1,*] and Dayang Laila Abang Abdul Majid [1]**

1. Department of Aerospace Engineering, Faculty of Engineering, Universiti Putra Malaysia,
   43400 Serdang, Selangor, Malaysia

*Correspondence: sivasanghari24@gmail.com

**Abstract:** The effects of stress concentration caused by grippers in a simple tensile testing of fine wire specimens might influence the reliable extraction of their mechanical properties. In line with this issue, the effectiveness of a snubbing gripper design for simple tensile test of fine wires was studied. Instron 3366 Universal Testing Machine with 5 kN load cell was used to apply uni-axial tension to two types of fine wire specimens: copper wire with diameter of 0.51 mm and shape memory alloy (SMA) wire, which is nickel-titanium (NiTi) wire with diameter of 0.31 mm. The snubbing gripper was applied to securely grasp the fine wires and the specimens were loaded until they fractured. The corresponding stress versus strain diagram was developed using data obtained from the Instron software to determine the ultimate tensile strength, which was then compared with the theoretical values obtained from the literatures. In general, the findings indicated that no slippage occurred at the fastened part between the gripper and the wire specimen. In addition, there was also longitudinally uniform elongation throughout the wire specimens, which proved there was a uniform stress distribution throughout the wires. Differences of the ultimate tensile strength value for the copper and NiTi wires with those in literatures were found to be 0.15% and 0.59%, respectively. Overall, the good agreement between experimental and theoretical stress versus strain diagrams has verified the proficiency of the snubbing gripper in grasping fine wire specimens for simple tensile tests.

**Keywords:** tensile testing; fine wire specimens; gripper; ultimate tensile stress; shape memory alloy

## 1. Introduction

Today, fine wires such as the carbon steel, copper, gold, aluminum, stainless steel, magnesium and nickel titanium shape memory alloy (SMA) wires are widely used in various fields including aerospace, robotics, automotive, medical devices, electrical devices, structures, civil and textile industries. The wires are progressively required to become much finer, approximately less than 1-mm diameter, mainly due to the reduction of weight, functionality and miniaturization of products that use them [1]. The progress of fine wires can be seen in the research work by Daitoh et al. [2] and Tarui et al. [3], in which they have developed steel wire with diameter of 0.02 mm and the tensile strength higher than 4 GPa. Furthermore, Britz et al. had succeeded in developing the nickel-titanium (NiTi) actuator wires with diameter between 0.25 mm and 0.5 mm, and with tensile strength of 200 MPa [4].

Simple tensile test on fine wire specimens is very important since it is utilized to determine material properties of these wires, especially their strength [5]. In tensile testing, strength of wires (or also known as tensile property) refers to the ability of the wires to resist loads from any pulling or stretching forces without rupture [5]. However, the extraction of tensile properties in tensile test for fine wire specimens is very sensitive and complicated due to exertion of stress by the grippers of the tensile testing machine, which could result in unreliable tensile test results [6]. Besides that, during the execution of tensile test, the fine wire specimen is in direct contact with the gripper and has the tendency to slip, thus affecting reliability of results from the tensile test [6]-[8]. To overcome the slippage issue of fine wire specimens, the most practical thing to do is to tighten the gripper such that the specimen is securely grasped by the gripper. However, care should be taken when tightening the fine wire specimen as over-tightening can lead to premature deformation of the specimen, which subsequently affects the validity of the extracted mechanical data from the conducted tensile test [6]-[8]. With this in mind, adaptive gripper design that is capable of preventing the slippage and has adjustable tightening level is considered in this study.

In reference to the current standards for tensile tests such as ASTM E8/E8M-13a [9], there is no specific requirement for tensile testing of wire specimens. The usage of direct gripper for tensile testing is inappropriate because the wire cannot be analysed due to slippage tendency. Therefore, to best meet the requirements of compliancy of a standard tensile test, a snubbing gripper with three parts (i.e. non-contact, contact and fastened parts) is designed. This snubbing gripper is designed in accordance to the specifications stated in ASTME8/E8M in relation to typical wire type specimens. It should be noted that the existing gripper provides greater strength in grasping specimens with various sizes such as dog-bone, bar, plate type, round and sheet type specimens that comes with large diameter [9]. However, this new snubbing gripper design is more proficient for use with small-diameter specimens, particularly fine wires with diameter of less than 1 mm. In this paper, the effectiveness of the snubbing gripper design is verified by assessing its performance in grasping through a simple tensile test of fine wire specimens. Two types of wire specimens applied in this study are the copper wire and the NiTi SMA wire. Stress-strain diagram is developed from the tensile test results while the mechanical properties such as ultimate tensile strength (UTS) are extracted from the tensile test machine. The obtained data is assessed through comparison with the published theoretical data in literatures to indicate whether the tensile test results from using the snubbing gripper are acceptably good or not.

## 2. Material and Methodology

### 2.1. Fine wire specimens

The materials used in this experimental work were round copper wire with diameter of 0.51 mm and round nickel titanium SMA wire with 0.31 mm in diameter. The length of both wire specimens is 200 mm. Copper wire is metal alloy that has copper as a principal component whereas NiTi SMA wire is a unique memory metal that remember their original shape after deformation. It should be noted that the copper wire is supplied by Shengqi Technology Metal Division while the nickel titanium SMA wire is supplied by Dynalloy, Inc. The technical properties of the materials are tabulated in Table 1.

Table 1: Technical Properties of Copper [10] and Nickel Titanium Wires [11]

| | **Copper wires** | **Nickel titanium wires** |
|---|---|---|
| **Density** | 8.96 g/cm3 | 6.45 g/cm3 |
| **Diameter** | 0.51 mm | 0.31 mm |
| **Melting point** | 1085 °C | 1300 °C |
| **Composition** | 99.9% copper | 50% Ni, 50%Ti |
| **Ultimate tensile strength** | 200 MPa [12] | 1000 MPa [13] |

### 2.2. Snubbing gripper design

To meet the functional requirements as recommended in ASTM E8/E8M for the application of fine wires specimens in tensile test, a snubbing gripper is designed and fabricated as shown in Figure 1.

This gripper is designed with dual functions: one is the nut-bolt fastener and another is the dimensional clamping as indicated in Figure 1(c). During the experiment, the nut-bolt fastener is used to grasp the wire securely for the test. It should be noted that the gripper is fabricated using aluminium and stainless-steel materials, and possesses the benefits of inherent compliancy as recommended in ASTM E8/E8M. This makes the gripper ideal to be used for securely grasping the fine wire foe tensile testing, particularly for wires with diameter of less than 1 mm.

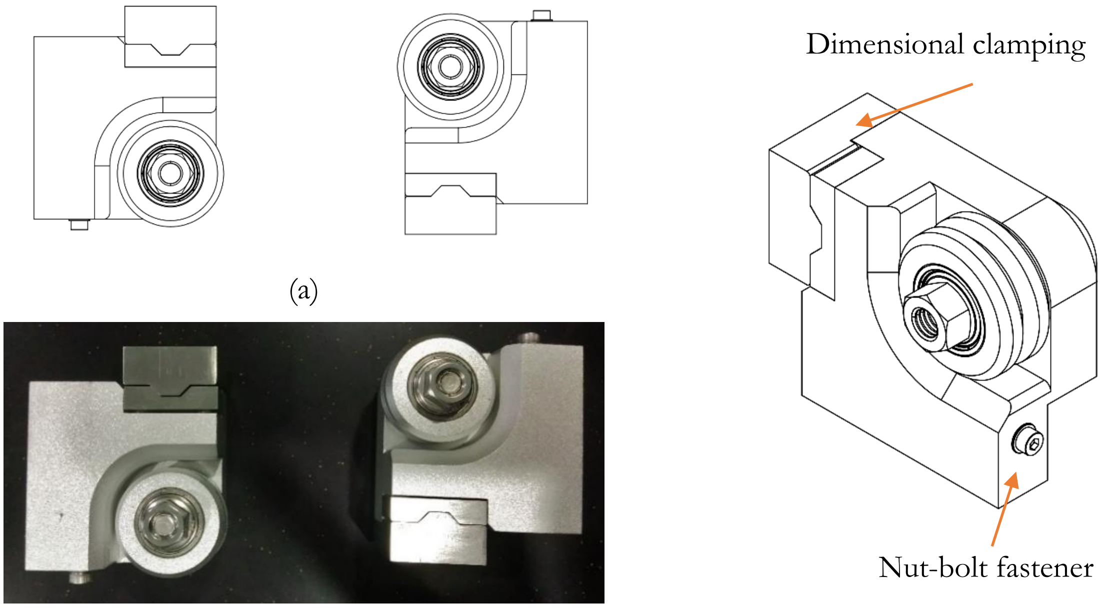

(a)

(b)

(c)

Figure 1: Snubbing gripper design: (a) SOLIDWORKS drawing of gripper, (b) physical fabricated gripper, (c) types of fasteners in gripper

### 2.3. Tensile testing

Tensile test was performed using the Instron 3366 Universal Testing Machine with 5 kN load cell at ambient room temperature. As recommended in ASTM E8/E8M, the strain rate used for copper wires was 2 mm/min. On the other hand, the strain rate of 0.2 mm/min was used for nickel titanium SMA wire as recommended in ASTM F2516. The uniaxial loading was applied until the specimen fail. Figure 2 depicts the image of the snubbing gripper, which was employed with the tensile testing machine during the experimental test. Note that the experiment was repeated three times for each type of wire (i.e. 3 specimens for each type of wire).

## 3. Results and Discussion

The constructed stress-strain diagrams for the copper and NiTi wires, which were loaded in tension until they fractured, are shown in Figure 3 and Figure 4, respectively. Previously, common shortcoming of the tensile test for fine wire specimens is that the stress transformation is non-uniform and slippage occurrences can be observed throughout the length of wire [12]. However, the results of stress-strain experimental data obtained from the conducted simple tensile test indicate that the fine wire specimens grasped by the snubbing gripper had longitudinally uniform elongation throughout the wire specimens. This further verify that there is a uniform and simultaneous stress transformation throughout the length of wire. The smooth uniform transformation also verifies that no slippage occurred during the tensile test, thus alleviate the effect of the stress concentration on the gripper.

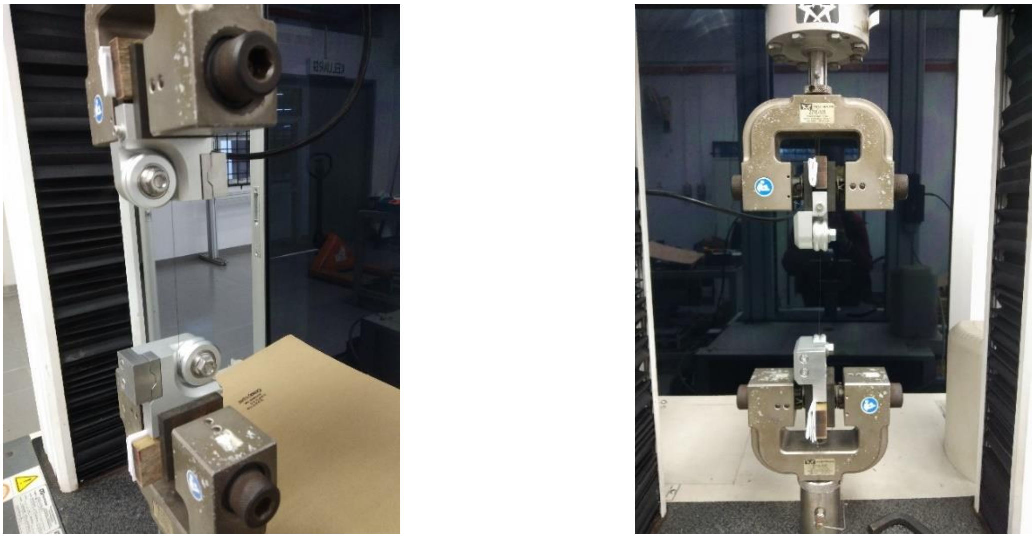

(a) (b)

Figure 2: Use of the snubbing gripper with the tensile testing machine: (a) side view of gripper placement, (b) front view of gripper placement

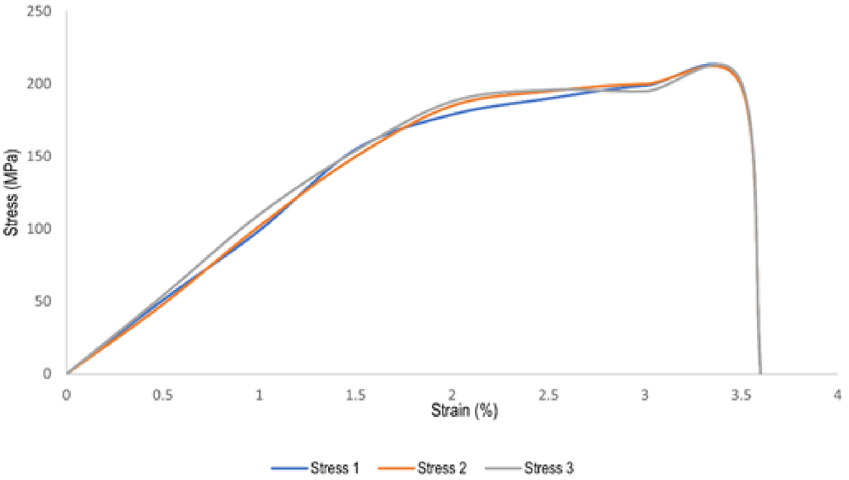

Figure 3: Stress-strain diagram of the copper wire loaded in tension until fracture

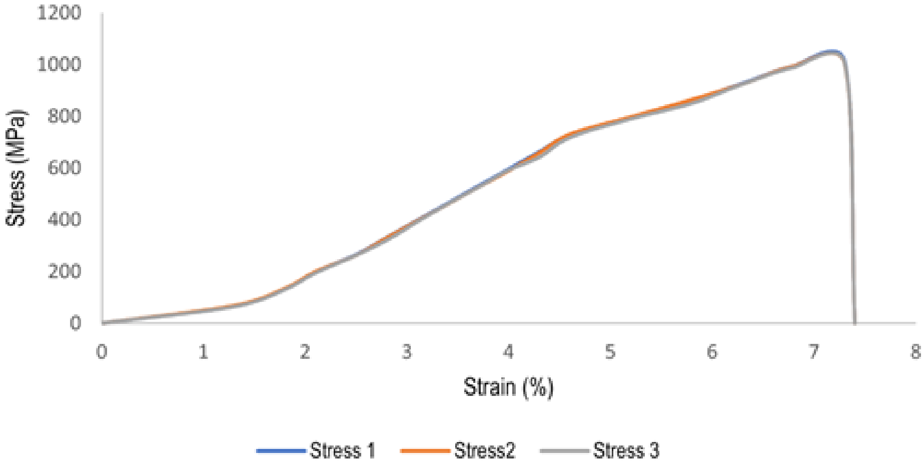

Figure 4: Stress-strain diagram of the NiTi wire loaded in tension until fracture

Moreover, it can also be observed that the use of the designed snubbing gripper is able to produce experimental results with reasonable accuracy in comparison to the present theoretical values for copper wires and NiTi wires as tabulated in Table 2. Krisha et al [13] in his research work had verified the UTS for copper alloy is 200 MPa whereas Brown [14] technical support officer from Dynalloy company had stated that the UTS for Flexinol NiTi wire can exceed 1000 MPa without cycle for a simple tensile test.

Table 2: Comparison of Experimental and Theoretical UTS for Copper Wires and NiTi Wires

| Properties | UTS 1 (MPa) | UTS 2 (MPa) | UTS 3 (MPa) | Average UTS (MPa) | Theoretical UTS (MPa) |
|---|---|---|---|---|---|
| **Copper Wires** | 200.7 | 198.6 | 201.7 | 200.3 | 200 [13] |
| **NiTi Wires** | 1009.9 | 1002.7 | 1005.1 | 1005.9 | 1000 [14] |

Table 3 presents the measurement error of UTS for both copper wires and NiTi wires between the values obtained from the conducted experimental testing and the theoretical values from the literatures. The errors for copper wire and NiTi wire are calculated to be 0.15% and 0.59%, respectively. It can be concluded that the measurement error is significantly smaller in this experimental work, hence helps to verify that the snubbing gripper designed is an ideal solution to securely grasp fine wire specimens in tensile test. This also suggests that mechanical properties extracted by employing this snubbing gripper during tensile tests of wire specimens are more accurate due to the loading results in a uniform stress distribution. Accordingly, it is reasonable that this snubbing gripper design not only alleviates the stress concentration exerted by gripper but also prevents slippage occurrences during the tensile test.

Table 3: Measurement error of UTS

| Properties | Average UTS (MPa) | Theoretical UTS (MPa) | Error (%) |
|---|---|---|---|
| **Copper Wires** | 200.3 | 200 [13] | 0.15 |
| **NiTi Wires** | 1005.9 | 1000 [14] | 0.59 |

## 4. Conclusion

In this paper, a simple tensile test of copper wire and NiTi wire specimens is conducted and studied. This research has verified that the snubbing gripper design is able to reliably grasp fine wire specimens securely and fulfill the requirements of the tensile test such as alleviating the stress concentration exerted by the gripper prior to the tensile test and preventing slippage caused by gripper during the tensile test. Furthermore, a good agreement is seen between the experimental and the theoretical stress versus strain diagram for the two types of wire specimens used in this study, thus further verifies the snubbing gripper is proficient in grasping fine wire specimens for simple tensile test. Future works includes testing the effectiveness of the snubbing gripper design to be used with decreasing diameter of wire specimens and also with different geometry shapes of wire specimens.

## Acknowledgement

The authors like to thank Robotic Space Technology for fabricating the gripper and also Strength of Material Laboratory at Universiti Putra Malaysia for permission to use the universal testing machine.

## References

[1] S. Gondo, S. Suzuki, M. Asakawa, K. Takemoto, K. Tashima and S. Kajino, 'Establishing a Simple and Reliable Method of Measuring Ductility of Fine Metal Wire', International Journal of Mechanical and Materials Engineering, vol. 13, no. 5, pp. 1-11, 2018.

[2] Y. Daitoh and T. Hamada, 'Microstructure of Heavily-deformed High Carbon Steel Wires', Tetsu-to-Hagan, vol. 86, no. 2, pp. 105–110, 2000.

[3] T. Tarui, N. Maruyama, and H. Tshiro, 'Cementite Decomposition in High Carbon Steel Wires', Tetsu-to-Hagan, vol. 91, no. 2, pp. 265–271, 2005.

[4] R. Britz and P. Motzki, 'Analysis and Evaluation of Bundled SMA Actuator Wires', Sensors and Actuators A: Physical, vol. 333, 2022.

[5] P. Liu, G. He and L. Wu, 'Uniaxial Tensile Stress–Strain Behavior of Entangled Steel Wire Material', Materials Science and Engineering: A, vol. 509, no. 1-2, pp. 69-75, 2009.

[6] A. Jamalimehr, H. Ravanbakhsh, M. Kadkhodaei and M. Kamrani, 'Investigation of Dog-Bone Geometry for Simple Tensile Test of Pseudoelastic Shape Memory Alloys', Iranian Journal of Science and Technology, Transactions of Mechanical Engineering, vol. 40, pp. 337–345, 2016.

[7] M. Kamarni and M. Kadkhodaei, 'An Investigation into the Simple Tensile Test of SMA Wires Considering Stress Concentration of Grippers', Journal of Materials Engineering and Performance, vol. 23, pp. 1114-1123, 2014.

[8] M. Kamrani and M. Kadhodaei, 'Investigation on Local and Global Behaviours of Pseudoelastic Shape Memory Wires in Simple Tensile Test considering Stress Concentration of Grippers', Journal of Intelligent Material System and Structure, vol. 27, no. 2, pp. 221-232, 2016.

[9] ASTM E8/E8M-13a (2013) Standard Test Methods for Tension Testing of Metallic Materials. ASTM International, West Conshohocken, PA, USA.

[10] Shengqi Technology Metal Division. (2019). Ultra-High Purity Single Crystal Copper Wire [Product Description]. Retrieved from https://www.sqtmetal.com/ultra-high-purity-products/high-purity-single-crystal-copper-

[11] DYNALLOY, Inc. (2023). Technical Characteristics of Flexinol [Actuator Wires]. Retrieved from https://www.dynalloy.com/pdfs/TCF1140.pdf

[12] R. Suhail, G. Amato and D. McCrum, 'Thermo-mechanical Characterisation of NiTi-based Shape Memory Alloy Wires for Civil Engineering Applications', Journal of Intelligent Material Systems and Structures, vol. 32, no. 20, pp. 1-17, 2021.

[13] S.C. Krishna, N. K. Gangwar, A. K. Jha, and B. Pant, 'On the Prediction of Strength from Hardness for Copper Alloys', Journal of Materials, vol. 2013, pp. 1-6, 2013.

[14] J. Brown (Personal Communication, December 19, 2022) Tensile Strength of Flexinol NiTi Wire.

JOURNAL OF AEROSPACE SOCIETY MALAYSIA

*ARTICLE*

# EFFECTS OF FLAPPING WING MICRO AIR VEHICLE'S PITCHING ANGLE ON STABILITY AT LOW REYNOLDS NUMBER

**Mohamed Mowhoub** [1] **and Ermira Junita Abdullah** [1,*]

1. Department of Aerospace Engineering, Faculty of Engineering, Universiti Putra Malaysia, 43400 Serdang, Selangor, Malaysia

*Correspondence: ermira@upm.edu.my

**Abstract:** The instability of flapping wing aircraft makes them difficult to control. As it is challenging to control and puts passengers at risk, it is not currently employed in modern aircraft technology. This study aims to analyze the aerodynamic coefficients of flapping wing aircraft at different flapping angles in order to understand their effects on the aircraft's stability. XFLR5 software was used to calculate the aerodynamics coefficients and longitudinal derivatives in different range of flapping angles from 40° to -40°. This range of flapping angles has been selected for the purpose of this study based on the physical limitations of a mechanical vehicle. Theoretically, an aircraft without a tail is unstable because the main function of a tail is to produce a moment that counters the moment produced by the wings to balance the aircraft. In the presented research, a model has been designed with and without tail, and modeled using XFLR5 to produce the aerodynamics coefficients. Then, MATLAB software was used to develop the longitudinal flight dynamics for the model. The results show that the longitudinal motion is stable for the range of flapping angle between 40° to -40°. The natural frequency increases as flapping angle changes from 0° to 40° and from 0° to -40°. In the meantime, for the short period mode's eigenvalue, the real part moves toward the origin as the flapping angle changes from 0° to 40° and from 0° to -40°. On the other hand, for the phugoid mode's eigenvalue, the real part moves away from the origin to the left half plane as the flapping angle changes from 0° to 40° and from 0° to -40°.

**Keywords:** flapping wing; MAV; aerodynamic coefficients; stability; flight dynamics

## 1. Introduction

In general, the aerospace industry is always evolving through implementation of new technologies into old and existing ones. It can be noted that the foundation of the industry is largely based on nature creatures such as birds, insects and others [1]. The flapping wing aircraft is an example of the earliest technologies that mankind has tried to make or replicate from nature. However, due to the complexities and challenges, flapping wing aircraft was not used and several other types of inventions such as fixed wing aircraft has been used instead because their efficiency [2]-[5]. Flapping wing aircraft is essentially difficult to develop because of inconsistency in terms of its stability. It is not implemented in today's aircraft technology due to limited understanding of its dynamics. With better understanding, an optimal controller can be developed to produce a safe flapping wing flight. To this effect, there are conducted researches that have demonstrated the benefits of using flapping wing, though implementation of such methods might be more suitable for the smaller-size micro air vehicles (MAVs) [6]-[11].

For flapping wing aircraft to find wider applications in the aerospace industry, such as for passenger transport missions, more studies are required to better understand its flight dynamics. With this notion, the research work presented in this paper is aimed to analyze the aerodynamic coefficients of flapping wing aircraft at different flapping angles. The knowledge gained from this study helps to establish their influence on the aircraft's stability and subsequently facilitates the design of a better controller for a safe flapping wing flight.

## 2. Methodology

In XFLR5 software, a flapping wing model was created based on the work by Bomphrey et al. [2]. The model was updated with Phoenix airfoil for the main wing section and NACA 0009 airfoil for the tail section. Once airfoils were specified and analyzed, the creation of the new plane model in XFLR5 was completed. It should be noted that the NACA 0009 airfoil was chosen since it is symmetrical and commonly recommended for the aircraft's tail section [12]. Figure 1 illustrates the isometric view of the designed plane model in XFRL5 and Table 1 lists the parameters of the model.

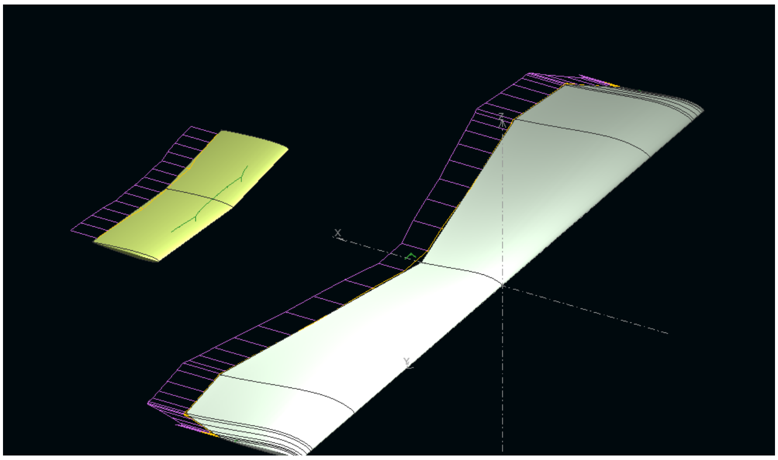

Figure 1: Isometric view of the designed plane model in XFLR5

Table 1: Parameters of model from XFLR5

| **Parameter** | **Value** |
|---|---|
| wingspan | 1.56 m |
| xyProj. Span | 1.56 m |
| Wing Area | 0.39 m$^2$ |
| xyProj. Area | 0.39 m$^2$ |
| Plane Mass | 2.25 kg |
| Wing Load | 5766.048 g/m$^2$ |
| Tail Volume | 0.445 |
| Root Chord | 0.18 m |
| MAC | 0.256 m |
| Tip Twist | 0 |
| Aspect Ratio | 6.237 |
| Taper Ratio | 1 |
| Root-Tip Sweep | 0 |
| $XNP = d(XC_p.C_l)/dc_l$ | 0.112 m |

Firstly, using XFLR5 software, aerodynamics and stability analyses were done on the entire model to obtain its aerodynamics coefficients at Reynolds number of 6 x $10^6$. Using the obtained aerodynamic coefficients and also previously estimated model parameters, the stability coefficients were computed. In this study, MATLAB software is applied in the calculation of the longitudinal and lateral coefficients based on formulas from Nelson [13]. Next, the stability derivatives were calculated. Subsequently, the corresponding state matrix, natural frequency and damping ratio were derived. These parameters were then utilized to simulate the plane model.

### 2.1. Equations of longitudinal motion

A first-order vector differential equation known as the state equation describes the natural form of aircraft motion. It is a mathematical representation of the aircraft's stability and control. The following Equation 1 describes the current condition of a trimmed aircraft, where *A* is the state coefficient matrix, $\vec{x}$ is the state vector, *B* is the driving matrix and $\vec{u}$ is the control vector [13].

$$\dot{x} = A\vec{x} + B\vec{u} \tag{1}$$

Moreover, the longitudinal state equation is given by the following Equation 2.

$$\begin{bmatrix} \dot{u} \\ \dot{w} \\ \dot{q} \\ \dot{\theta} \end{bmatrix} = \begin{bmatrix} X_u & X_w & 0 & -g \\ Z_u & Z_w & U_o & 0 \\ M_u & M_w & M_q & 0 \\ 0 & 0 & 1 & 0 \end{bmatrix} \begin{bmatrix} u \\ w \\ q \\ \theta \end{bmatrix} + \begin{bmatrix} X_\eta \\ Z_\eta \\ M_\eta \\ 0 \end{bmatrix} \eta \tag{2}$$

To use this state equation, the coefficients are first needed to find the longitudinal derivatives [12]. In general, the longitudinal derivatives can be attributed to changes in forward speed, pitching velocity and also time rate of change of angle of attack. Firstly, changes in the aircraft's forward speed will also alter its drag, lift and pitching moments. Plus, the aircraft's thrust is also a function of its forward speed. Meanwhile, the derivatives due to pitching velocity correspond to the change in the z-force and pitching moment coefficients caused by the pitching velocity, which is represented by stability coefficients, $C_{zq}$ and $C_{mq}$. The aircraft's pitching motion affects the aerodynamic properties of both wing and horizontal tail. In most cases, the wing contribution pales in comparison to that of the tail. On the other hand, the derivatives due to time rate of change of angle of attack relate to the lag in wing's downwash reaching the tail section and causing the stability coefficients below to increase. The circulation around the wing will change as its angle of attack varies. The downwash at the tail is altered by the change in circulation. However, the change takes a finite amount of time to occur. All in all, after calculating the coefficients, the longitudinal derivatives can be derived and the longitudinal state equation is obtained [13].

### 2.2. Validation study

In order to show that the steps and process followed in this study were correct, an initial case study was conducted for validation purposes. This validation study was made based on the presented case of Cessna 172 aircraft wing that was published by Hidayat et al. [14]. The wing model, which has NACA 2412 airfoil cross-sectional shape, was constructed in XFLR5 and it is as shown in Figure 2. The wing model was then analysed in XFLR5 under the same analysis settings as those specified in the reference literature. In this case, the Mach number was set to 0.19 and the range of Reynolds number was between $6 \times 10^6$ to $6.5 \times 10^6$, with increment of 500,000.

The analysis results from XFLR5 in the form of the plot of lift coefficient versus angle of attack is presented in Figure 3(a) while the one from the published reference is depicted in Figure 3(b). It can be observed that the two results are essentially consistent and greatly in line with each other, which is taken to validate the adequacy of steps and process used in this study. With this notion, the same methodology was applied in the analysis of the designed plane model that was the main focus of this study.

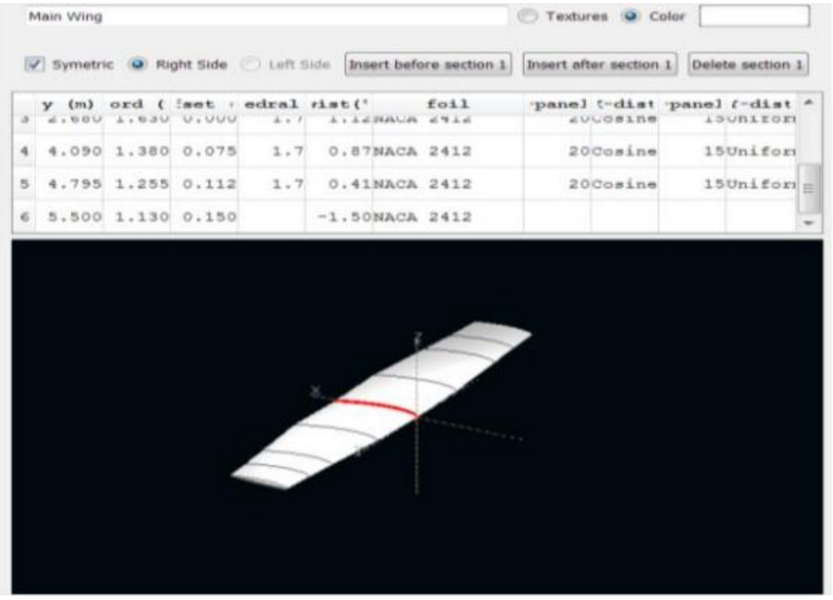

| | y (m) | ord ( | !set | edral | rist(' | foil | panel | t-dist | panel | (-dist |
|---|---|---|---|---|---|---|---|---|---|---|
| 3 | 2.680 | 1.630 | 0.000 | 1.7 | 1.12 | NACA 2412 | 20 | Cosine | 15 | Unifor |
| 4 | 4.090 | 1.380 | 0.075 | 1.7 | 0.87 | NACA 2412 | 20 | Cosine | 15 | Unifor |
| 5 | 4.795 | 1.255 | 0.112 | 1.7 | 0.41 | NACA 2412 | 20 | Cosine | 15 | Unifor |
| 6 | 5.500 | 1.130 | 0.150 | | -1.50 | NACA 2412 | | | | |

Figure 2: Constructed Cessna 172 aircraft wing model based on the study by Hidayat et al. [14]

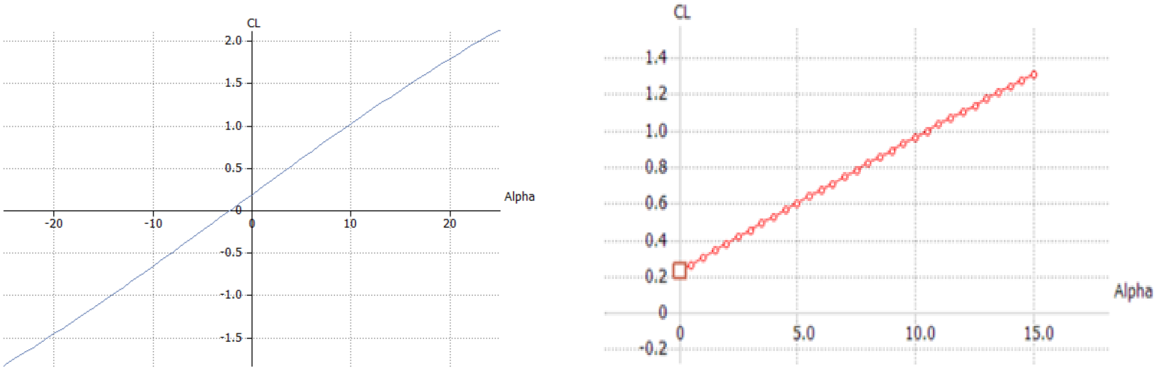

(a)

(b)

Figure 3: Plot of lift coefficient versus angle of attack from: (a) validation study in XFLR5, (b) reference literature by Hidayat et al. [14]

## 3. Results and Discussion

Figure 4 shows the airfoil analysis results for both the Phoenix and NACA 0009 airfoils from the XFLR5 software. In this figure, the result for Phoenix airfoil is marked by red color whereas those for the NACA 0009 airfoil is indicated by blue color. Figure 4(a) depicts plot of lift coefficient, $C_l$ versus angle of attack, $\alpha$. It essentially shows how these two airfoils behave in three main regions: linear, non-linear and post stall regions. As can be observed, value of $C_l$ initially increases linearly with increment in $\alpha$. However, at some point, $C_l$ starts to decrease with further increase of $\alpha$ until it reaches the stall region, where the value of $C_l$ decreases drastically. At this stall region, the wing has more pressure on its upper surface than its lower surface. For the Phoenix airfoil, it starts losing lift and enters stall region at $\alpha = 11°$. At the same angle of attack, referring to Figure 4(b), it can be seen that the drag coefficient, $C_d$ increases exponentially, which results in higher drag and decrease in the ratio of $C_l/C_d$ as presented in Figure 4(c). Similar observations can be made with regard to the results for NACA 0009 airfoil, which appears to stall at lower angle of attack than that for the Phoenix airfoil.

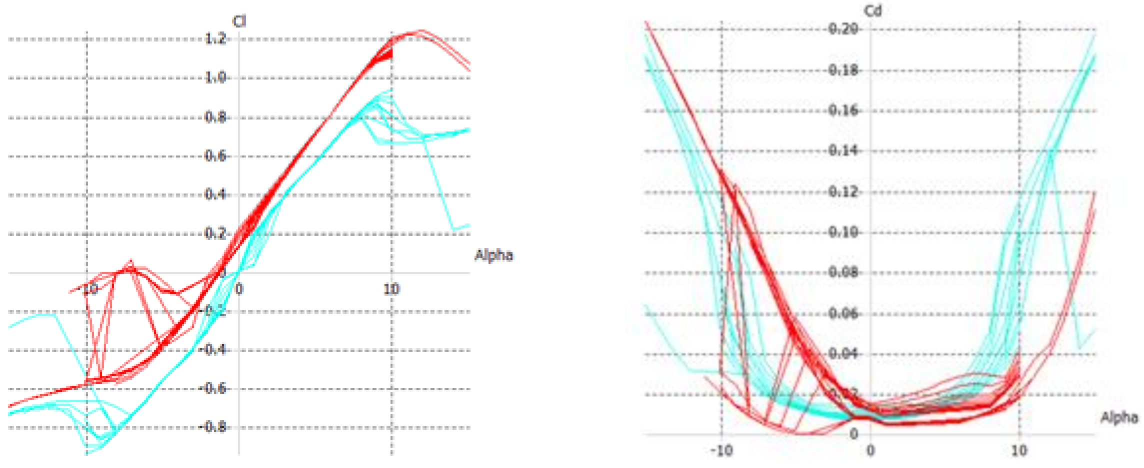

(a) $C_l$ versus α (b) $C_d$ versus α

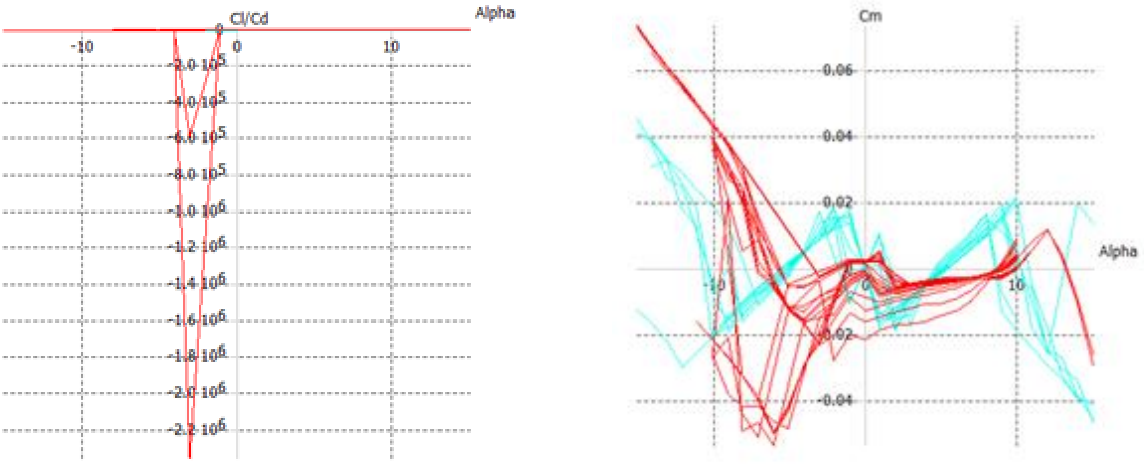

(c) $C_l/C_d$ versus α (d) $C_m$ versus α

Figure 4: Airfoil analysis results for Phoenix airfoil (red) and NACA 0009 airfoil (blue)

On the other hand, the analysis results from XFLR5 on the designed model are presented in Figure 5. Of particular interest in terms of stability is the plot of the moment coefficient, $C_M$ versus α that is shown in Figure 5(d). It can be observed that the slope of this $C_M$ versus α plot is positive, which means that the plane model fulfills the longitudinal static stability criterion and can be trimmed. However, the plane cannot be trimmed at positive angles of attack and this condition is reflected by the negative value of angle of attack where the line plot intercepts the α-axis. Meanwhile, looking at Figure 5(c) that depicts the plot of $C_L/C_D$ versus α, the value of $C_L/C_D$ starts to decrease after $\alpha = 5°$ and this implies that plane is maybe close to entering its stall region where drag increases and lift decreases. Using the aerodynamics data obtained from XFRL5, the longitudinal coefficients were calculated using MATLAB. For flapping angle of 0°, the calculated values are tabulated in Table 2. These coefficients were then applied to obtain the dynamics model, natural frequency, damping ratio and eigenvalues. Finally, with this information, the stability of the model could be determined.

For longitudinal dynamics, the eigenvalues are found to be -5.5233 + 34.9633i, -5.5233 – 34.9633i, -0.0285 + 0.2335i, and -0.0285 – 0.2335i. It can be observed that the eigenvalues are complex and the real parts of the root are negative. This indicates that the system is dynamically stable, which means that if the system was given an initial disturbance, the motion would be sinusoidal but would not grow with time and therefore it is considered to be stable. The natural frequency for the short period and phugoid mode were found to be 35.3969 and 0.2352, respectively. In the meantime, damping ratios for the short period and phugoid mode were found to be 0.1560 and 0.1210, respectively.

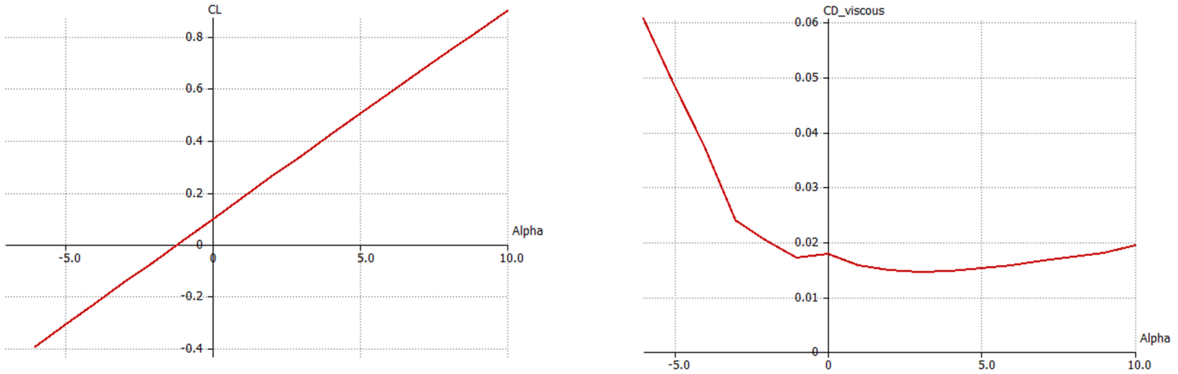

(a) $C_L$ versus α (b) $C_{D\_viscous}$ versus α

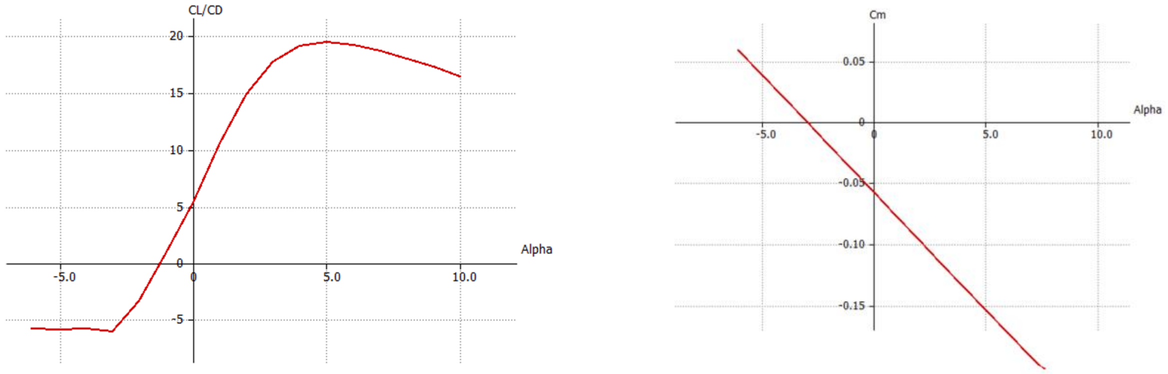

(c) $C_L/C_D$ versus α (d) $C_M$ versus α

Figure 5: Aerodynamics analysis results of the designed plane model

Table 2: Longitudinal coefficients at flapping angle of 0° as obtained from MATLAB

| **Stability Coefficients** | **Value** |
|---|---|
| $C_{x_u}$ | -0.0540 |
| $C_{X_a}$ | 0.0543 |
| $C_{z_u}$ | -0.1440 |
| $C_{\mathrm{Z}_\alpha}$ | -4.6680 |
| $C_{\mathbf{Z}_{\dot{\alpha}}}$ | -1.3491 |
| $C_{z_q}$ | -2.8437 |
| $C_{Z_{\delta_e}}$ | -0.2427 |
| $C_{m_a}$ | -2.5456 |
| $C_{m_{\dot{\alpha}}}$ | -3.1619 |
| $C_{m_q}$ | -6.6650 |
| $C_{m\delta_e}$ | -0.5688 |

Moreover, Figure 6 presents the summary for the longitudinal motion at 0° pitching. The first plot in Figure 6(a) shows the behavior of forward speed, u versus time, t. It shows that the amplitude of u is decreasing as time increases. In this case, the amplitude decreases to -40 in 10 seconds, which might indicate that aircraft is not generally stable in terms of forward speed. This situation might be because the plane model does not have a propulsive system since it is a glider and changes in thrust is expected. Meanwhile Figure 6(b) shows the change of vertical speed, w with time, t. The plot indicates that the amplitude of w oscillates between 0 and -0.4 at the start for roughly less than 1 second before becoming stable with minimum change in amplitude. In the meantime, Figure 6(c) shows the plot of pitch change, q versus time, t. It can be observed from the plot that the amplitude of q becomes constant after nearly half a second. Its amplitude appears to oscillate between 2 to -6 at the beginning and then decease to 0. Lastly, the final plot in Figure 6(d) shows the change in pitch angle, α against time, t. It can be seen in the plot that the change in amplitude of α is very small, which ranges between 0 to -0.4. Furthermore, the amplitude oscillates between -0.2 to -0.4 in about 8 seconds, which is considered very stable.

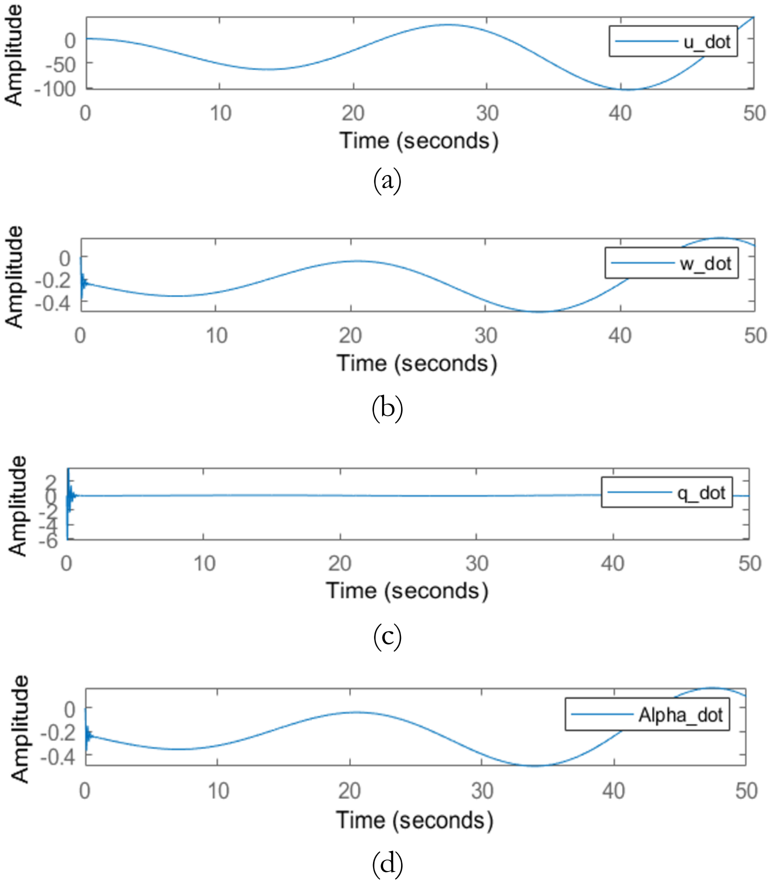

(a)

(b)

(c)

(d)

Figure 6: Longitudinal response for pitching angle of 0°

The same analysis was repeated for other flapping angles from -40° to 40° and the comparison of obtained results in terms of the natural frequency in longitudinal long period mode is shown in Figure 7. It can be observed that the highest frequency of about 35 rad/sec was recorded at 0° angle while the lowest frequency of 21 rad/sec was recorded at both 40° and -40° angles. In general, it can be seen that as the flapping angle increases, the natural frequency decreases. On the other hand, Figure 8 shows the comparison of natural frequency for short period mode at different flapping angles. In short, the angles of 0°, 10° and 20° appear to have the same frequency of 0.235 rad/sec while all other angles have higher frequency with maximum of 0.266 rad/sec for flapping angles of 40° and -40°. Subsequently, essentially similar observations for the comparison of damping ratios at different flapping angles were obtained as illustrated by Figure 9 and Figure 10. Furthermore, Table 3 tabulates the corresponding longitudinal eigenvalues for long and short period modes. It can be seen that all of the eigenvalues have a positive real root, which indicates that the aircraft is stable. Additionally, as flapping angle moves further from 0°, the eigenvalues come closer to the origin point, which is 0.

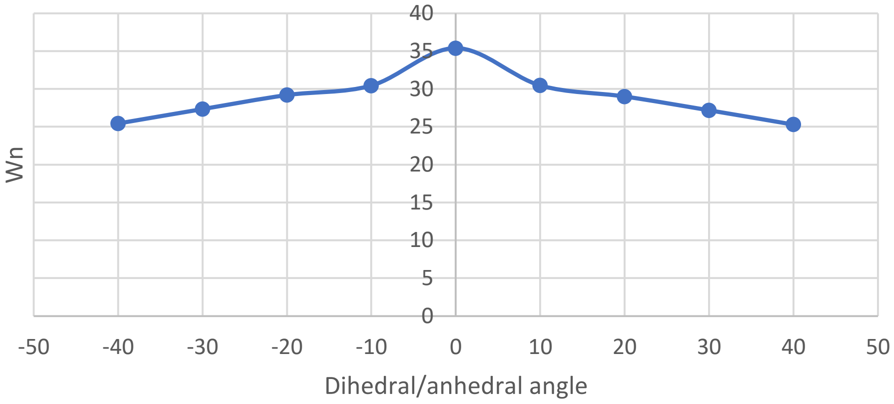

Figure 7: Natural frequency comparison for longitudinal long period

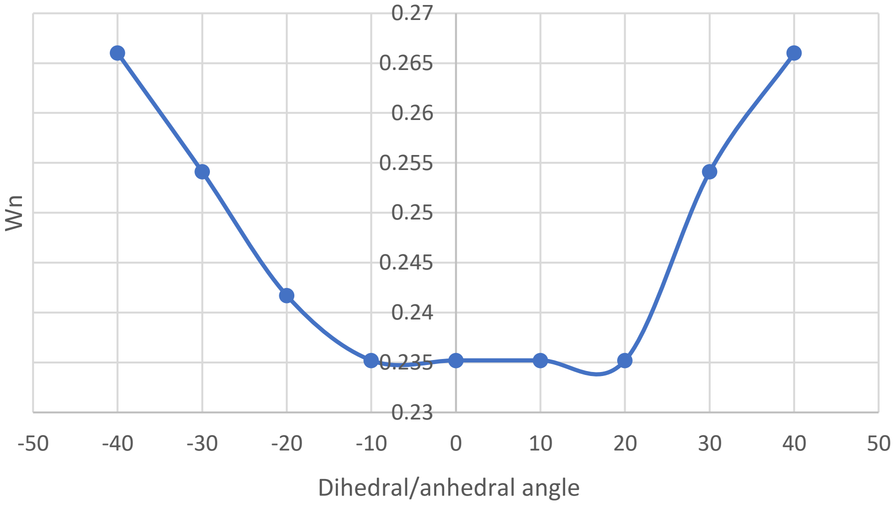

Figure 8: Natural frequency comparison for longitudinal short period

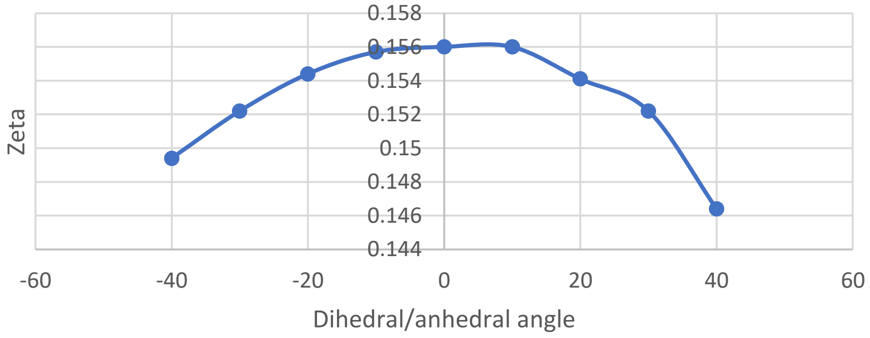

Figure 9: Damping ratio comparison for longitudinal long period

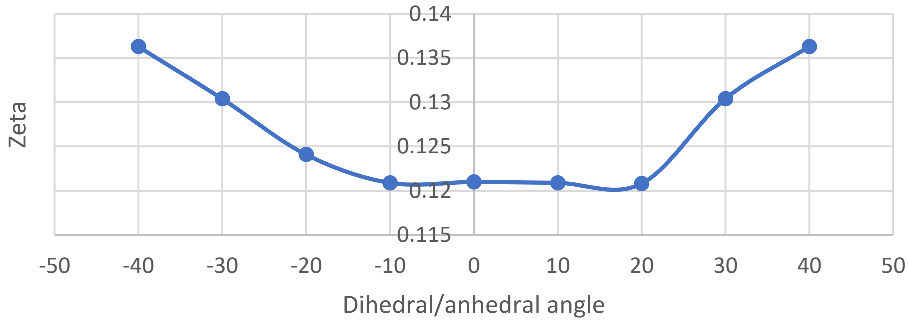

Figure 10: Damping ratio comparison for longitudinal short period

Table 3: Longitudinal eigenvalues for all considered flapping angles

| Angle (°) | Mode | Eigenvalues |
|---|---|---|
| 40 | Short period | -3.7795 ± 25.1072i |
| | Phugoid | -0.0363 ± 0.2635i |
| 30 | Short period | -4.1378 ± 26.8753i |
| | Phugoid | -0.0331 ± 0.252i |
| 20 | Short period | -4.4718 ± 28.6654i |
| | Phugoid | -0.0284 ± 0.2335i |
| 10 | Short period | -4.7547 ± 30.1062i |
| | Phugoid | -0.0284 ± 0.2335i |
| 0 | Short period | -5.5233 ± 34.9633i |
| | Phugoid | -0.0285 ± 0.2335i |
| -10 | Short period | -4.741 ± 30.0785i |
| | Phugoid | -0.0284 ± 0.2335i |
| -20 | Short period | -4.5081 ± 28.8478i |
| | Phugoid | -0.03 ± 0.2398i |
| -30 | Short period | -4.1629 ± 27.0252i |
| | Phugoid | -0.0331 ± 0.0252i |
| -40 | Short period | -3.8021 ± 25.1573i |
| | Phugoid | -0.0363 ± 0.2635i |

## 4. Conclusion

In this study, a model of flapping wing plane has been constructed using Phoenix and NACA 0009 airfoils as the cross-sectional shape of the main wing and tail sections, respectively. This flapping wing vehicle's model requires the tail section to provide balance as the main function of this tail section is to produce a moment that counters the moment that is produced by the main wing section. Based on the conducted stability analysis, it was demonstrated that this model could perform well for flapping wing vehicles. The results show that the longitudinal motion is stable for the range of flapping angle between 40° to -40°. The natural frequency is shown to increase as the flapping angle increases from 0° to 40° and -40°. For the short period mode's eigenvalue, the real part moves towards the origin as the flapping angle increases from 0° to 40° and -40°. On the other hand, for the phugoid mode's eigenvalue, the real part is shown to move away from the origin to the left half plane as the flapping angle is increased from 0° to 40° and -40°. The subsequent future work can be done on evaluating the dynamics stability of the flapping wing model at a lower Reynolds number in the range of $10^4$ to $10^5$. The sizing and shape of the airfoils can also be explored to find the optimal design for use in MAVs at low Reynolds number. This will provide designers with more understanding and a range of suitable options in designing MAVs.

**References**

[1] N. Slosar, 'Avians to Airplanes: Biomimicry in Flight and Wing Design', Berkeley Scientific Journal, vol. 25. No. 2, pp. 25-27, 2021.

[2] R. J. Bomphrey, T. Nakata, P. Henningsson and H. T. Lin, 'Flight of the Dragonflies and Damselflies', Philosophical Transactions of the Royal Society B: Biological Sciences, vol. 371, no. 1704, 20150389, 2016.

[3] M. F. Platzer, K. D. Jones, J. Young and J. C. S. Lai, 'Flapping Wing Aerodynamics: Progress and Challenges', AIAA Journal, vol. 46, no. 9, pp. 2136-2149, 2008.

[4] R. H. Siddique, Y. J. Donie, G. Gomard, S. Yalamanchili, T. Merdzhanova, U. Lemmer and H. Hölscher, 'Bioinspired Phase-separated Disordered Nanostructures for Thin Photovoltaic Absorbers', Science Advances, vol. 3, no. 10, e1700232, 2017.

[5] F. Mazhar and S. I. Ali Shah, 'On the Unsteady Aerodynamics and Design of Flapping Wing Vehicles', International Bhurban Conference on Applied Sciences and Technology, Islamabad, Pakistan, 14-18 January, 2020.

[6] C. P. Du, J. X. Xu and Y. Zheng, 'Modeling and Control of a Dragonfly-like Micro Aerial Vehicle', Advances in Robotics and Automation, vol. S2, no. 2, 006, 2015.

[7] J. Chahl, N. Chitsaz, B. McIvor, T. Ogunwa, J. Kok, T. McIntyre and E. Abdullah. 'Biomimetic Drones Inspired by Dragonflies Will Require a Systems Based Approach and Insights from Biology', Drones, vol. 5, no. 2, 24, 2021.

[8] M. Hassanalian, G. Throneberry and A. Abdelkefi, 'Investigation on the Planform and Kinematic Optimization of Bio-inspired Nano Air Vehicles for Hovering Applications', Meccanica, vol. 53, pp. 2273-2286, 2018.

[9] T. Ogunwa, B. McIvor, N. Awang Jumat, E. Abdullah and J. Chahl, 'Longitudinal Actuated Abdomen Control for Energy Efficient Flight of Insects', Energies, vol. 13, no. 20, 5480, 2020.

[10] B. Liang and M. Sun, 'Dynamic Flight Stability of a Hovering Model Dragonfly', Journal of Theoretical Biology, vol. 348, pp. 100-112, 2014.

[11] N. Marimuthu, E. J. Abdullah, D. L. A. Majid and F. I. Romli, 'Conceptual Design of Flapping Wing Using Shape Memory Alloy Actuator for Micro Unmanned Aerial Vehicle', Applied Mechanics and Materials, vol. 629, pp. 152-157, 2014.

[12] M. S. Sarker, S. Panday, M. Rasel, M. A. Salam, K. M. Faisal and T. H. Farabi, 'Detail Design of Empennage of an Unmanned Aerial Vehicle', AIP Conference Proceedings, vol. 1919, no. 1, 020033, 2017.

[13] R. C. Nelson, Flight Stability and Automatic Control, WCB/McGraw Hill, 1998.

[14] F. T. Hidayat, B. Rabeta, F. F. Prodi, "Analisis Pengaruh Winglet Pada Sayap Pesawat Cessna 172 Menggunakan Perangkat Lunak XFLR5', Jurnal Teknologi Kedirgantaraan, vol. 5, no. 1, pp. 48–54, 2020.

# ASSESSMENT OF AIRCRAFT PASSENGERS' COMFORT WITH VARYING SEAT PITCH

**Nur Hidayah Ismail[1], Nadia Hanani Ahmad Habibillah[1] and Fairuz Izzuddin Romli[1, *]**

1. Department of Aerospace Engineering, Faculty of Engineering, Universiti Putra Malaysia, 43400 Serdang, Selangor, Malaysia
* Correspondence: fairuz_ir@upm.edu.my

**Abstract:** In-flight comfort has become an important issue among aircraft passengers. Over the years, the seat pitch used in the passenger cabin has been gradually reduced, which is believed to be the main source of in-flight discomfort among the passengers. A sitting comfort experiment is conducted in this study using available aircraft cabin mock-up at the Aerospace Design Simulation Laboratory, Universiti Putra Malaysia, Malaysia. 30 volunteers participated in the experiment whereby they assigned their level of sitting comfort for five different seat pitch arrangements: 66.04 cm (26 in.), 73.66 cm (29 in.), 81.28 cm (32 in.), 88.90 cm (35 in.) and also 96.52 cm (38 in.). Their sitting comfort rating is assigned using the standard 5-point Likert scale and the collected data is then statistically analyzed using the MINITAB software. From the conducted statistical analysis, it is concluded that the seat pitch setting has a very significant effect on the passengers' in-flight sitting comfort.

**Keywords:** seat pitch; flight comfort; statistical analysis; aircraft cabin; sitting comfort

## 1. Introduction

Air transportation industry is progressively growing worldwide over the years as more people are using aircraft as their selected travel option. This situation also increases the level of market competition between airlines since air travelers are now provided with plethora of air travel services to choose from. The quality of offered services by the airlines has been indicated as the key consideration by passengers in their travel selection, which ultimately becomes the critical competitive factor for the airlines [1]-[2]. In general, a good quality flight service is often taken as the one that fulfills the needs and/or expectancy of the passengers [3]. Among the factors that directly contribute towards passengers' perception on the quality level of flight services provided by the airlines, in-flight comfort is one of the important criteria. As indicated in Ref. [4], in-flight sitting comfort is a key element for in-flight service quality. Therefore, it is imperative for airlines to ensure that their aircraft cabin is capable to provide adequate comfort for their passengers throughout the flight trip.

In general, comfort is defined as the pleasant state or relaxed feeling of the human body in response to the surrounding physical environment while discomfort is the opposite unpleasant feeling [5]. It has also been argued that comfort and discomfort are separate sensations, which indicates that the absence of discomfort does not necessarily mean comfort [6]. To date, many complaints of in-flight discomforts by passengers can be attributed to limited legroom available at their seat, which is directly linked to the setting of the cabin seat pitch. From ergonomists' point of view, seat pitch is a critical comfort element in aircraft cabin design as it influences the easiness of passengers adopting a comfortable sitting posture during flight [7]. As depicted in Figure 1, seat pitch is a measure of the distance between one point of the seat to the exact same point of the seat in front or behind it. These days, airlines usually reduce the cabin seat pitch of their aircraft to further accommodate more passengers inside the cabin per flight in order to maintain profitability amid rising flight operation costs. It can be observed that the aircraft seat pitch, particularly in the economy class seating arrangements, has been gradually reduced over the years.

For instance, the seat pitch for many American airlines used to be around 78.74 to 88.90 cm (31 to 35 in.) in the 1970s and that has generally reduced to only 71.12 cm (28 in.) in most of these airlines today [8]. A smaller seat pitch subsequently means much lower legroom available for passengers at their seat, contributing to their discomfort feeling during flight.

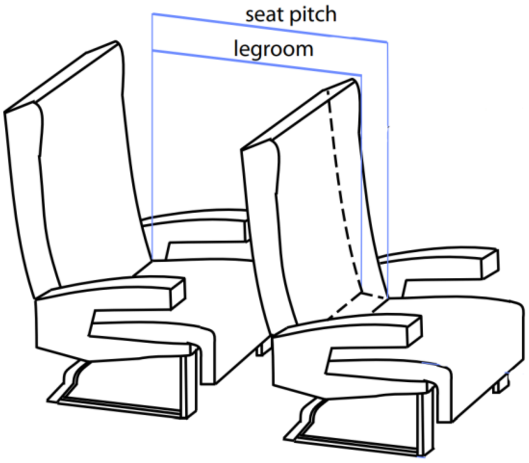

Figure 1: Seat pitch and legroom measurement [9]

With increasing importance of passengers' in-flight comfort toward the market competitiveness of offered flight services, it is thus necessary for airlines to strike a balance between operational profitability and perception of their service quality by their passengers. Among others, this means that the seat pitch in their passenger cabin seating arrangement has to be set by also considering the passengers' comfort. In view of this, the study presented in this paper aims to assess the underlying relationship between in-flight comfort and seat pitch, with a focus on Malaysian population. By understanding this relationship, airlines can better design their aircraft cabin arrangements such that their passengers are provided with adequate level of flight comfort.

## 2. Methodology

An aircraft sitting comfort experiment is conducted using a cabin mock-up available in Aerospace Design and Simulation Laboratory, Universiti Putra Malaysia. The cabin mock-up is as shown in Figure 2. Voluntary participants for the experiment are contacted through promotional 'call for participants' postings on several social media outlets such as WhatsApp and Facebook. The main selection criteria for the participants include that they must be Malaysian citizen and must have previous experiences in using commercial flight services prior to the experiment. Overall, among all of the responses received, 30 volunteers have been down selected and invited to participate in the experiment.

For the comfort sitting experiment, the participants are asked to individually sit in the aircraft cabin mock-up, one at a time. Each participant sat through five different parts of the experiment where the seat pitch is adjusted at the end of each part, from 66.04 cm to 96.52 cm (26 in. to 38 in.) Assessment of their perceived comfort level in each part of the experiment, hence the comfort of sitting at several different seat pitch settings, is provided by participants at the end of each part. This assessment is done using a prepared comfort survey that is adopted from another study in Ref. [10]. However, considering the differences between how the sitting comfort experiment is conducted in this study and the reference study, only the elements tabulated in Table 1 are included into the comfort assessment survey. In the meantime, standard 5-point Likert scale rating shown in Table 2 is applied in the assessment. It is noted that comfort assessment is also often associated with activity-based evaluation. However, for this study, the aim is to mainly have a general comfort assessment and thus the participants are given the freedom to conduct whatever activities that they wanted during the sitting experiment. This means that the rating that they provided is of general aspect in terms of their overall feeling and is not associated with any specific in-flight activities such as eating or using a laptop.

Figure 2: Aircraft cabin mock-up used in this study

Table 1: Assessment elements of in-flight sitting comfort (adopted from [10])

| **Comfort Assessment Categories** | **Survey Elements** |
|---|---|
| Postural Sensation | • I can easily adopt a comfortable sitting posture<br>• I can easily change from one sitting posture to another |
| Spatial Perception | • I don't feel restricted<br>• I don't feel restricted by the distance of the seating row<br>• I don't feel like sitting in front of a wall |
| Privacy | • I don't feel lost because of the distance of the seating row |
| Present Mood | • I don't feel stressed out because of the distance of the seating row |

Table 2: Likert scale for comfort assessment

| **Rating** | **Description** |
|---|---|
| 1 | • I strongly disagree with the statement |
| 2 | • I disagree with the statement |
| 3 | • I feel neutral with the statement |
| 4 | • I agree with the statement |
| 5 | • I strongly agree with the statement |

## 3. Results and Discussion

Table 3 presents descriptive statistics of the obtained results from the sitting comfort experiment. In addition, using the collected experimental data, correlation analysis between seat pitch and comfort assessment criteria is conducted using statistical software, MINITAB. Correlation analysis is a standard statistical method that is used to study the strength of relationship between two variables or parameters [11]. In this study, it is of high interest to observe the strength of influence of seat pitch on the comfort of passengers, which is reflected by its relationship to the different aspects of comfort assessment. The results of correlation analysis are tabulated in Table 4, which shows the Pearson correlation coefficient that measures the strength of the linear relationship between the seat pitch and the comfort rating.

Table 3: Average comfort ratings

| Comfort Assessment Categories | Seat Pitch (in cm) | | | | |
|---|---|---|---|---|---|
| | **66.04** | **73.66** | **81.28** | **88.90** | **96.52** |
| Postural Sensation | 1.40 | 2.63 | 4.07 | 4.57 | 4.85 |
| Spatial Perception | 1.27 | 2.30 | 3.20 | 4.09 | 4.24 |
| Privacy | 4.43 | 4.03 | 3.73 | 2.97 | 2.80 |
| Present Mood | 1.33 | 2.33 | 3.23 | 3.97 | 4.47 |

Table 4: Correlation analysis between seat pitch and comfort assessment

| Comfort Assessment Categories | Assessment Elements | Correlation Coefficient with Seat Pitch |
|---|---|---|
| Postural Sensation | I can easily adopt a comfortable sitting posture | 0.824 |
| | I can easily change from one sitting posture to another | 0.850 |
| Spatial Perception | I don’t feel restricted | 0.832 |
| | I don’t feel restricted by distance of seating row | 0.703 |
| | I don’t feel like sitting in front of a wall | 0.747 |
| Privacy | I don’t feel lost with distance of seating row | -0.476 |
| Present Mood | I don’t feel stressed out with distance of seating row | 0.802 |

It can be seen from Table 3 that average comfort ratings for postural sensation, spatial perception and present mood appear to monotonously increase with increasing seat pitch. In contrast, for privacy, its comfort rating appears to decrease with the increasing seat pitch. As the seat pitch is increased, the available legroom has also increases. During the experiment, with increased legroom, it can be observed that the participants could easily adopt their own preferred sitting postures and this has made them felt more comfortable. Furthermore, as the distance between the rows becomes larger, the participants also felt more unrestricted by their limited seating space, particularly since the back of seat in front of them was not too close on their face. This situation apparently also helped to improve on their present mood as reflected by the trend of the assigned comfort rating with seat pitch for this assessment category. On contrary, having a small seat pitch seems to allow more privacy for the participants at their seat. As the distance between the rows becomes larger, the level of privacy also diminishes since there is now more available room or space at their seat. This allows a higher probability that other passengers can invade their personal space at their seat and also makes the passengers feel more exposed. All in all, based on the presented ratings in Table 3, it can be taken that the best compromise is probably at a seat pitch of

32 inches where all of the assigned ratings for each of the comfort assessment elements are all above 3, which is at acceptable or neutral level.

From the resultant correlation coefficient tabulated in Table 4, it can be taken that the relationship of seat pitch and comfort is highly correlated. This means that the setting of the seat pitch can greatly influence the passengers' comfort from several different aspects. The positive correlation coefficient is indicating that the relationship is in tandem or in the same direction, i.e. increasing seat pitch will also increase the level of comfort in that aspect. This situation is true for all elements of postural sensation, spatial perception and also present mood, which are in line with the observed trend of assigned comfort rating in Table 3. In the meantime, parallel to the opposite trend that is observed in Table 3 for privacy assessment, the correlation coefficient between seat pitch and privacy is negative. Furthermore, value of the coefficient is also relatively low, meaning that the assigned comfort rating by participants in this aspect at each seat pitch setting was rather inconsistent to each other. This can be taken to indicate that the participants may have fairly different ideas of privacy. While increasing seat pitch generally reduces their sense of privacy, the perceived effects on their sitting comfort were considerably at different levels. More discussion on the possibly subjective and personal nature of this passengers' comfort assessment can also be found in Ref. [12].

## 4. Conclusion

Passengers' comfort today has become a great competitive service factor between airlines and it is therefore important for airlines to be able to provide adequate comfort level to their passengers during flight. The findings in this study has shown that the setting of the cabin seat pitch has a great impact to the level of sitting comfort to the passengers, which is reflected by the high value correlation coefficient. A higher seat pitch will improve postural sensation, spatial perception and present mood of passengers, though it might also reduce their perception of privacy level. A compromise may need to be considered and in this study, the seat pitch of 81.28 cm (32 in.) could be taken to obtain a favorable comfort rating simultaneously for all assessment criteria. As an initial study to highlight the significant influence of seat pitch towards the aircraft passengers' comfort, this objective has been successfully achieved. However, moving forward, more detailed study should be conducted to appropriately establish and estimate the effects of seat pitch on the passengers' comfort level, especially by also including other comfort factors such as passengers' anthropometric measures into account.

## Acknowledgement

The authors acknowledge the funding of this research from Ministry of Higher Education Malaysia through their Fundamental Research Grant Scheme: FRGS/1/2018/TK09/UPM/2/1 (Vot: 5540074).

## References

[1] J. Wang, Z.-R. Xiang, J.-Y. Zhi, J.-P. Chen, S.-J. He, and Y. Du, 'Assessment Method for Civil Aircraft Cabin Comfort: Contributing Factors, Dissatisfaction Indicators and Degrees of Influence', International Journal of Industrial Ergonomics, vol. 81, 103045, 2021.

[2] R. Hussain, A. A. Nasser, and Y. K. Hussain, 'Service Quality and Customer Satisfaction of a UAE-based Airline: An Empirical Investigation', Journal of Air Transport Management, vol. 42, pp. 167-175, 2015.

[3] N. Maisarah, D. K. M. Hung, N. Syakirah, M. A. Hanif, A. Bella, R. Pandey, R. F. Almuhaini, and M. A. Quttainah, 'Customer Satisfaction Towards Service Quality: A Study of Malindo Air', International Journal of Tourism and Hospitality in Asia Pacific, vol. 3, no. 3, pp. 40-51, 2020.

[4] K. Singaravelu and V. P. Amuthanayaki, 'A Study on Service Quality and Passenger Satisfaction on Indian Airlines', Journal of Commerce and Trade, vol. 12, no. 2, pp. 106-115, 2017.

[5] P. Vink and S. Hallbeck, 'Comfort and Discomfort Studies Demonstrate the Need for a New Model', Applied Ergonomics, vol. 43, no. 2, pp. 271-276, 2012.

[6] M. G. Helander and L. Zhang, 'Field Studies of Comfort and Discomfort in Sitting', Ergonomics, vol. 40, no. 9, pp. 895-915, 1997.

[7] H. Pei, S. Yu, M. Ding, and Z. Bai, 'Aircraft Passenger Comfort Based on Muscle Activation and Perceived Discomfort During Long Flight', Aerospace Medicine and Human Performance, vol. 91, no. 5, pp. 1-6, 2020.

[8] S. R. Winter, 'Government Seat Pitch Regulation of Commercial Airlines: A Multi-Study of Consumer Perception', Collegiate Aviation Review International, vol. 37, no. 2, pp. 1-15, 2019.

[9] G. Nadadur and M. B. Parkinson, 'Using Designing for Human Variability to Optimize Aircraft Seat Layout', SAE International Journal of Passenger Cars – Mechanical Systems, vol. 2, no. 1, pp. 1641-1648, 2009.

[10] F. Kremser, F. Guenzkofer, C. Sedlmeier, O. Sabbah, and K. Bengler, 'Aircraft Seating Comfort: The Influence of Seat Pitch on Passengers' Well-being', Work, vol. 41, pp. 4936-4942, 2012.

[11] R. Ceravolo, G. Coletta, G. Miraglia, and F. Palma, 'Statistical Correlation Between Environmental Time Series and Data from Long-term Monitoring of Buildings', Mechanical Systems and Signal Processing, vol. 152, 107460, 2021.

[12] N. Ahmadpour, G. Lindgaard, J.-M. Robert, and B. Pownall, 'The Thematic Structure of Passenger Comfort Experience and Its Relationship to the Context Features in the Aircraft Cabin', Ergonomics, vol. 57, no. 6, pp. 801-815, 2014.

# COMPUTATIONAL AERODYNAMICS ANALYSIS ON PITCHING MOMENT USING DUCTED FAN OVER FLAT PLATE FOR HIGH ALTITUDE PLATFORM STATION

**Nur Liyana Sabrina Muhd Arif [1], Hidayatullah Mohammad Ali [1, *]**
**and Azmin Shakrine Mohd Rafie [1]**

1. Department of Aerospace Engineering, Faculty of Engineering, Universiti Putra Malaysia, 43400 Serdang, Selangor, Malaysia

*Correspondence: hidayatmaddali@gmail.com

**Abstract:** The CyFlaP is a new invention that operates based on the principle of Magnus effect. It is essentially developed to be applied as unmanned aerial vehicle (UAV) and high altitude platform station (HAPS) for surveillance purposes that can fly in the stratosphere region. In previous study of CyFlaP, the presence of a moment force acting at the centre of its body is shown to affect its stability during flight. To address this problem, this study explores the placement of a ducted fan on both sides of the CyFlaP, which are intended to provide thrust and also help to stabilize it. For the latter purpose, a flat plate is installed at the back of the ducted fan such that the ejected flow behind it can be used to produce a lift force on the flat plate, which is then projected to counter existing pitching moment on the CyFlaP. Simulation analysis of the flow on the plate located behind the rotating ducted fan is conducted using computational fluid dynamics (CFD) software in ANSYS Workbench 2021. The simulation analysis is done with different rotational ducted fan speeds up to 5000 RPM for three cases of flat plate's aspect ratio at different angles of attack ranging from 0° to 15° with fixed free stream velocity of 5 m/s. The results indicate that the increase in the aspect ratio of the flat plate will decrease the generated lift force. In contrast, the lift force is increased with higher rotational speed of the ducted fan and larger angle of attack of the plate. However, on the whole, it is found that implementing a flat plate behind the ducted fan is inadequate to oppose the existing acting moment force on the CyFlaP and hence the search for better design solution to resolve the issue is still ongoing.

**Keywords:** ANSYS; aerodynamics analysis; pitching moment; ducted fan; high altitude platform station

## 1. Introduction

Back in 1961, stemming from curiosity of Isaac Newton about spinning tennis ball, the discovery of a new physics law known as Magnus effect was made. In general, Magnus effect theory is named after a German physicist and chemist, Gustav Magnus and it relates to the generation of lateral force on a spinning cylinder in fluid when the spinning body is in relative motion with the fluid [1]-[4]. This discovery led to many inventions and applications but not all of them were successful, which might be attributed to insufficient knowledge of this aerodynamic phenomenon and unsuitable use of material at that time. Nevertheless, the potential advantages of this principle in producing higher lift forces in comparison to airfoil-based lifting systems have continued to motivate its application in the creation of devices for various purposes including for harvesting wind energy, propelling and steering vessels, and also lifting an airplane [1].

Future unmanned aerial vehicle (UAV) technologies can take advantages of a high lift coefficient from the usage of the spinning cylinder, where the spinning cylinder can replace the airfoil as the wing. An exemplary invention that is designed with the Magnus effect concept is the cyclorotor, which has been shown to be able to provide hovering and also attain forward speed that is faster than the current helicopters [5]. In addition, another invention using this Magnus effect principle is known as D-Dalus, which is built around a four-cyclogyro rotor propulsion system combined with an aerodynamic winged body to add lift in forward flight. The D-Dalus design has been essentially demonstrated to be capable of vertical take-off and landing (VTOL), and hovering [6]. Furthermore, of particular interest in this study is the Cylinder-Flat Plate-Cylinder (CyFlaP). Based on Magnus effect principle, a double-rotating cylinder placed at both sides of the CyFlaP has demonstrated its capability to produce lift during flight. In general, CyFlaP is developed as one of the technologies for UAV and high altitude platform station (HAPS) for surveillance missions in aerospace applications. The previous computational fluid dynamics (CFD) study on CyFlaP found that it generates the most lift at 1000 RPM with clockwise-to-clockwise (CW-CW) rotational direction of the spinning cylinders [7]–[8]. In addition, lift generation capability of CyFlaP has also been demonstrated in an experimental study that is conducted in the wind tunnel [8]. However, it is also found that the generated lift force from the double-rotating cylinder creates moment force that is acting at the centre of the CyFlaP, which affects its stability and can cause undesired body rotations during flight [8]. This issue has to be resolved, especially if it is to be used as HAPS that should require low flight control measures as it is often intended for employment in remote areas for long time period.

Continuing on previous studies, the work in this paper explores the solution to stability problem of CyFlaP by incorporating a ducted fan and a flat plate. As shown in Figure 1, the ducted fan is placed on both sides of the CyFlaP. Apart from thrust provision, the ejected flow behind the ducted fan is also utilised to generate lift force on the flat plate located at the back of it. It is believed that the lift produced on the flat plate can counter back the undesired moment force that is acting on the CyFlaP. Under this notion, the objective of this study is to analyse the capability of this proposed mechanism to counter the existing pitching moment of the CyFlaP through computational fluid dynamics (CFD) simulation analysis.

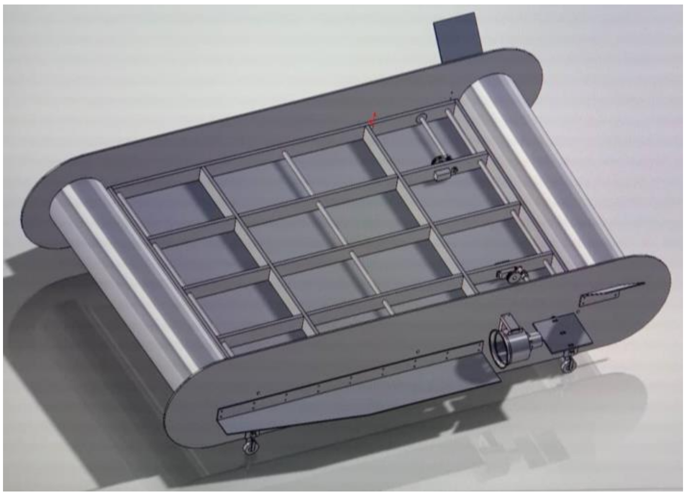

Figure 1: The proposed CyFlaP design

## 2. Methodology

The methodology used for this research work is described in the following sub-sections. This offers insight into the methods applied in this research.

### 2.1. Geometry design of CyFlaP modeling

Computer-aided design (CAD) model for the proposed CyFlaP design is constructed as illustrated in Figure 2. On the other hand, the drawing for the ducted fan design model is depicted in Figure 3. It should be noted that the ducted fan model is based on the FMS 70-mm Ducted Fan Jet EDF design. In this study, the model is simplified to reduce computational time in getting the result and to increase the meshing quality. The ducted fan is modelled using SolidWorks according to the real dimensions of FMS 70-mm model.

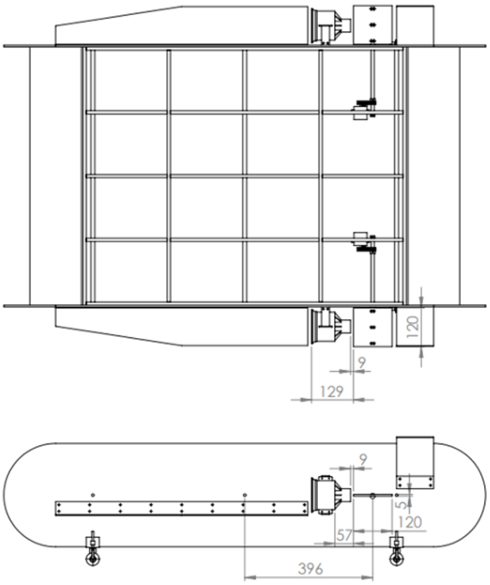

Figure 2: CAD drawing of the proposed CyFlaP design model

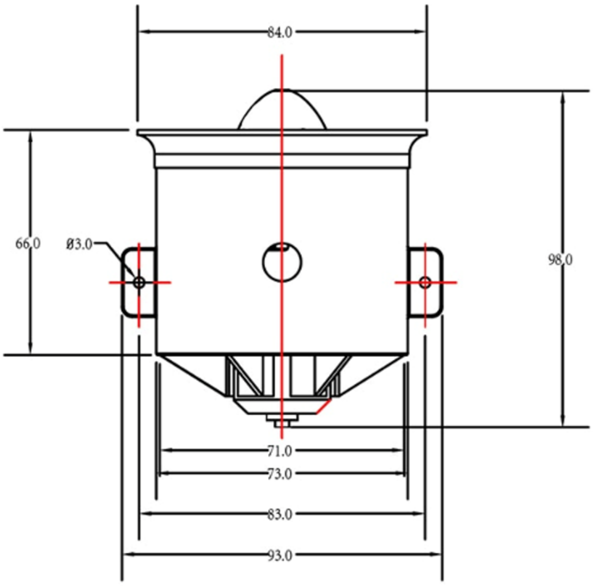

Figure 3: CAD drawing of the FMS EDF 70-mm ducted fan model

For CFD simulation analysis, the flow domain, flat plate and rotating zone are constructed using the design modeller. The stationary domain enclosing the ducted fan and the flat plate is illustrated in Figure 4. For this simulation, since the blades' rotation is simulated using sliding mesh techniques, the rotating zone is modelled as a cylinder body that enclosed the blade as depicted in Figure 5.

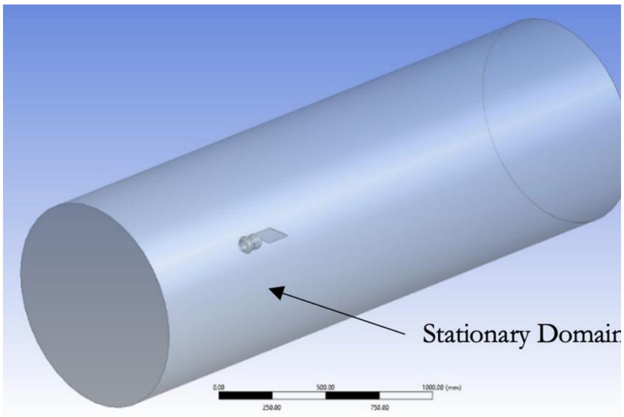

Figure 4: Stationary domain enclosing the ducted fan and flat plate

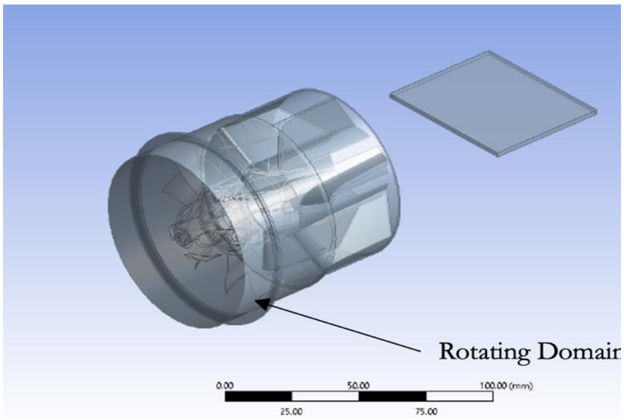

Figure 5: Rotating domain enclosing the blade

Moreover, since this study is focused on the amount of generated pitching moment to counter the existing moment on the CyFlaP design, several parameters can be taken into consideration to increase its value, either from the aspects of the flat plate or the ducted fan. In this study, the attention is placed on the effects from the variation of aspect ratio of the flat plate, rotational speed of the ducted fan and also angle of attack of the CyFlaP on the generated pitching moment. The magnitude of the moment force is calculated by taking the lift force value from the simulation results and multiplying it with the distance between the centre of CyFlaP to the centre of pressure of the flat plate. In this case study, the different aspect ratios of the flat plate would give different positions of the centre of pressure, which is located at quarter chord of the flat plate [9]. Consequently, the moment calculated is multiplied by two as there are two ducted fans attached to the CyFlaP. It should be noted that the changes in aspect ratio of the flat plate in this study are accomplished by only changing the length of its chord. Meanwhile, the width of the flat plate is kept constant at 0.12 m and the distance of the ducted fan to the flat plate is also fixed at 0.009 m. Moreover, the standard sea level data property is fixed throughout the simulation process.

## 2.2. Grid and mesh generation

The grid generations refer to the methods of defining numerical mesh throughout the entire system that will be modelled. The grid used for the CFD simulations will also have an impact on the calculation time and the accuracy of the results. In this study, the simulation analysis is performed in the presence of a wind tunnel as the flow domain in order to mimic the experimental condition more accurately. The computational meshes are made up of unstructured meshes and inflation is added on the flat plate with the y-plus (y+) value being less than 1 as shown in Figure 6 and Figure 7. As for boundary conditions, the named selection settings are used to name every boundary: the inlet as ‘velocity-inlet’, the outlet as ‘pressure-outlet’, the blade as ‘wall’, the flat plate as ‘wall’, the interior domain and the rotating body both as ‘interior’, and lastly the wall as ‘wall’.

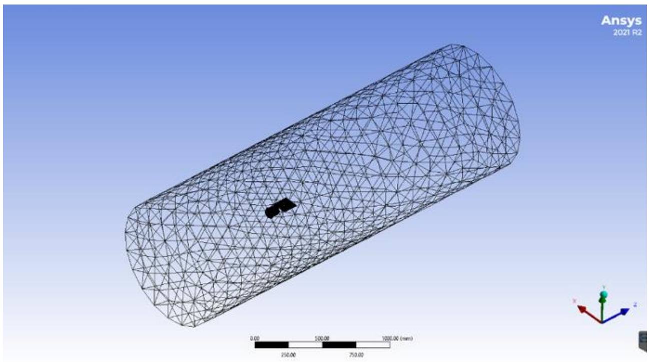

Figure 6: Unstructured mesh of fluid domain and model

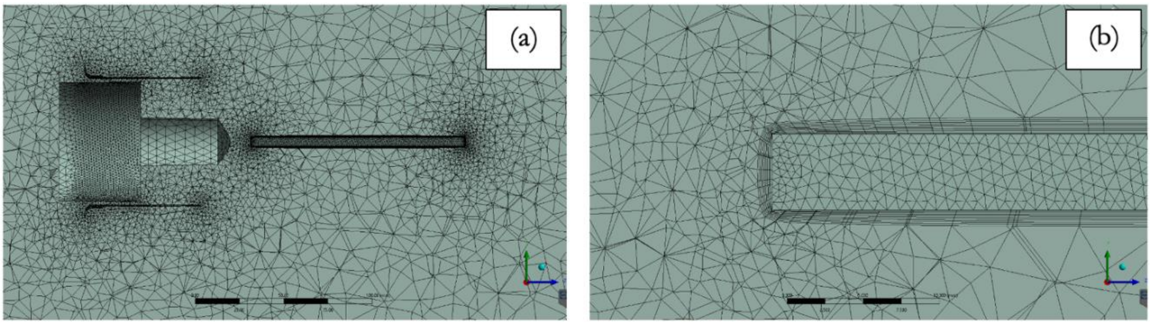

Figure 7: Mesh setup for: (a) ducted fan and flat plate model, (b) near wall surface of flat plate

Further details on the mesh and inflations settings are listed in Table 1. For this study, the skewness is characterized as the variation of the cell shape between the equilateral cell shape and the interpretation of the cell volume. Highly skewed cells might reduce the precision and make the solution unstable. On the other hand, orthogonality relates to vector mechanics and low orthogonality is not recommended in meshing processes. Based on Table 1, the skewness and orthogonal quality stated can be taken to lie within the generally acceptable value spectrum of mesh quality recommendations.

Table 1: Meshing settings for this study

| **Mesh Details** | |
|---|---|
| Growth rate | 1.2 |
| Defeature size | 8.29e-04 m |
| Curvature minimum size | 1.66e-03 m |
| Curvature normal angle | 18.0 ° |
| Capture Curvature | Yes |
| Capture Proximity | Yes |
| Smoothing | High |
| Skewness | 0.82911 |
| Orthogonal quality | 0.17089 |
| **Inflations Details** | |
| Inflation option | First Layer Thickness |
| Maximum layer | 10 |
| Growth rate | 1.05 |

## 2.3. Solver settings

After a good mesh quality is obtained, appropriate solver settings must be set up before calculating the solution in the CFD solver interface. The ideal configuration displayed in Table 2 is considered to scrutinize the numerical solution. There are five main settings in the setup process: general, model, cell zone condition, reference values and spatial discretization. In general setting, transient flow simulation is set due to occurrence of turbulent flow from the rotation of the fan's blades. The reference value is based on the velocity inlet of 5 m/s wind speed condition at a sea level condition [9]. In addition, the sliding mesh method is selected to make a moving mesh of the rotating body region since this is known as the most accurate way of simulating flows in multiple moving frames due to the rotor interaction in an unsteady flow region. Furthermore, the spatial discretization uses second-order upwind method. In the meantime, the transient formulation term is discretized using second-order implicit format and the SIMPLE algorithm is used to solve the discrete algebraic equations [10].

K-ω model was applied in previous study that was conducted to analyse the characteristics of fluid flow around rotating configurations in the proposed Re regime [11]. The two-equation model with two additional transport equations describing the attributes of turbulent flows is used to approximate the Reynolds-averaged Navier–Stokes (RANS) equations. The first transported variable, K is for turbulent kinetic energy while the second transported variable, ω is for rate of specific dissipation. On the other hand, Shear Stress Transport (SST) K-ω turbulence model has been formulated, which combines the standard k-ω and k-ε turbulence models [12]-[16]. The boundary layer's wake region employs the normal k-ω turbulence model whereas the sublayer of the wall boundary layer employs k-ε turbulence model. Concurrently, in adverse pressure gradient flows, the SST model is typically used as it can demonstrate accurate turbulence prediction and separating flows. Therefore, SST k-ω turbulence model is applied in this study to solve the governing equations while considering turbulent flow field in the rotating blade.

Table 2: Solver settings for this study

| **General** | |
|---|---|
| Type | Pressure-based |
| Velocity formulation | Absolute |
| Time | Transient |
| **Model** | |
| Viscous | SST K-omega (K-ω) |
| **Cell Zone Condition** | |
| Rotating body | Mesh motion |
| **References Value** | |
| Density (kg/m$^3$) | 1.225 |
| Pressure (pascal) | 101325 |
| Temperature (K) | 228.16 |
| Velocity (m/s) | 5 |
| Viscosity (kg/m-s) | 1.789e-05 |
| Scheme | SIMPLE |
| **Spatial Discretization** | |
| Pressure | Second Order |
| Momentum | Second Order Upwind |
| Turbulent kinetic energy | Second Order Upwind |
| Specific dissipation rate | Second Order Upwind |
| Transient formulation | Second Order Implicit |

### 2.4. Validation study

A validation study on solver settings of the CFD analysis process is conducted before proceeding with the actual case study. An identical ducted fan is modelled according to the one used in Cho et al. [10] with similar computational domain and solver settings as stated in their paper. Following this, the analysis of its thrust performance is then compared with the validation model to validate the veracity of the solver setting that will be used for the real model, which is presented in Figure 8.

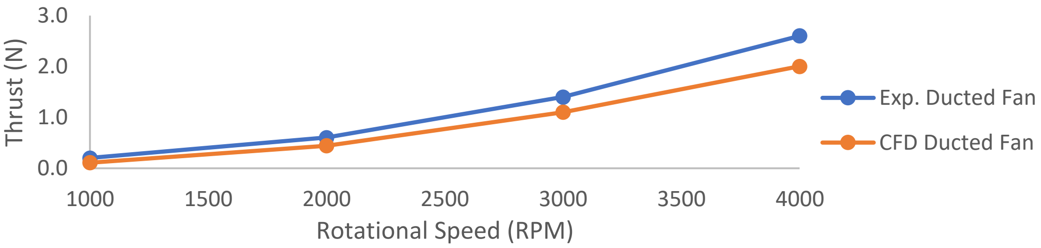

Figure 8: Validation of ducted fan thrust as compared to experimental data from Cho et al. [10]

As can be observed in Figure 8, the percentage error is below 25% owing to a slight contradiction in the undetailed dimension of the ducted fan region and blade angle from the paper by Cho et al. [10].

In addition, computational meshes from Cho et al. [10] consist of 0.97 million unstructured tetra meshes and 0.98 million structured prism meshes for both the inner and outer cylinders of the domain body. Unfortunately, number of meshes used in this validation study could not resemble the specified meshes due to limitation of computer capability, which contributes to increasing distinction in the percentage error of thrust performance in conjunction with increasing RPM value. Nevertheless, similar trend of the results is observed and the solver settings used in this study can be considered as appropriate to be applied for the real simulation case study.

## 3. Results and Discussion

In short, this computational study involves three variables throughout the simulation analysis. The varying values are angle of attack, rotational speed of the ducted fan and aspect ratio of the flat plate. The angle of attack is varied at four different values: 0°, 5°, 10° and 15°. Meanwhile, three values of the rotational speed for the ducted fan are considered in this study, which are 1000 RPM, 3000 RPM and also 5000 RPM. Last but not least, aspect ratio of the flat plate is varied at three different values, which are 0.5, 1.0 and 1.5. As previously mentioned, the variation of the aspect ratio is made by changing the chord length of the flat plate while maintaining its width length. The obtained results are presented and discussed in following sub-sections.

### 3.1. Effects of angle of attack on the lift produced

By observation of both Figure 9 and Figure 10, a steady increase of generated lift force by the flat plate can be generally seen as the angle of attack is increased. In Figure 9, with constant aspect ratio of flat plate of 0.5 and rotational speed of the ducted fan of 1000 RPM, the generated lift force at angle of attack of 5° is 0.037 N, which then increases up to 0.09 N at 10° and finally becomes 0.16 N at 15°. In fact, the magnitude of the generated lift is also increased with increasing angle of attack and rotational speed of the ducted fan when the aspect ratio of the flat plate is maintained at 0.5. Likewise, a similar trend of generated lift force with increasing angle of attack is displayed in Figure 10, where the rotational speed of the ducted fan is kept constant at 1000 RPM while the value of aspect ratio of the flat plate is varied. It can be noted from Figure 10 that, with higher aspect ratio of flat plate for the same rotational speed of the ducted fan, the magnitude of lift force is reduced at each angle of attack.

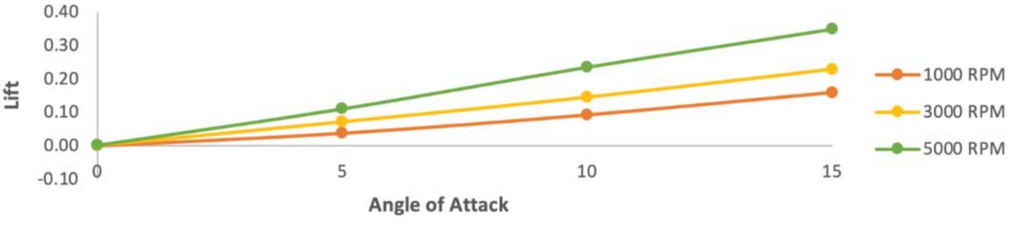

Figure 9: Lift (in N) versus angle of attack (in °) for flat plate's aspect ratio of 0.5 at various rotational speed of the ducted fan

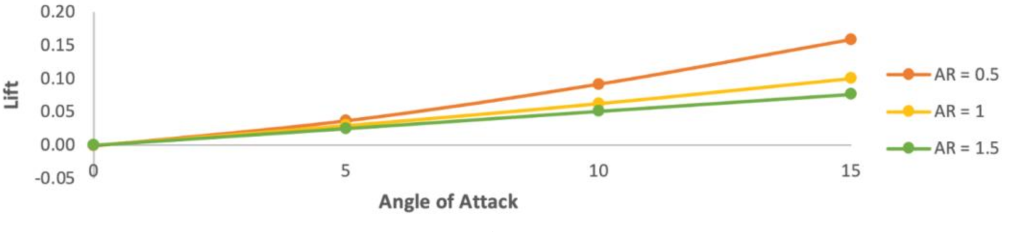

Figure 10: Lift (in N) versus angle of attack (in °) for rotational ducted fan speed of 1000 RPM at various aspect ratio of the flat plate

In general, this result correlates with the study of aerodynamic forces on a flat plate. Aerodynamic forces such as lift and drag will act on any objects moving through the airstream. For flat plates that are inclined to the direction of the airflow, pressure of the air above the plate decreases while the pressure beneath it increases. This results in net pressure experienced by the plate, attempting to force it upwards [17]. Thus, the larger the inclination angle, the higher the force acting on the plate, which is consistent with the trend observed in both previous Figure 9 and Figure 10.

### 3.2. Effects of rotational speed of the ducted fan on the moment produced

The net lift force generated by the flat plate in the simulation can be used to calculate the moment value at a specified distance with respect to its aspect ratio. It should be noted that the distance between the flat plate and the centre of CyFlaP includes the gap between the ducted fan and the plate, and also the distance from the centre of pressure of the plate. The distance of the centre of pressure is different according to the aspect ratio. Figure 11, Figure 12 and also Figure 13 illustrate the calculated moments at different rotational speeds from the two engines to counter the pitching moment of the CyFlaP.

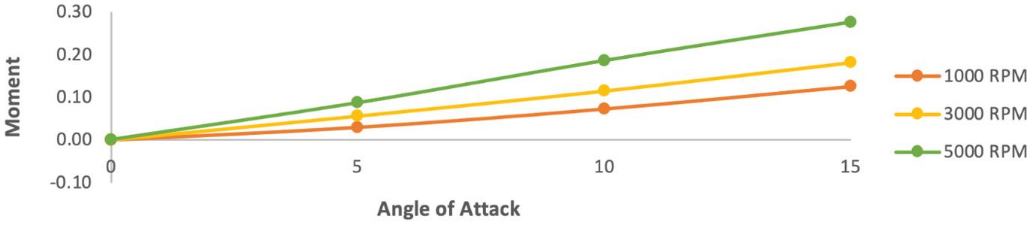

Figure 11: Moment (in Nm) versus angle of attack (in °) for flat plate's aspect ratio of 0.5 at various rotational speed of the ducted fan

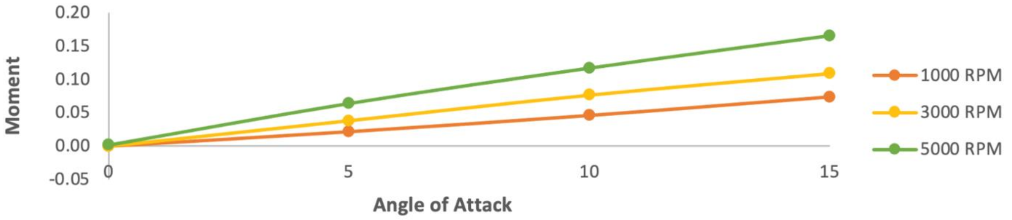

Figure 12: Moment (in Nm) versus angle of attack (in °) for flat plate's aspect ratio of 1.0 at various rotational speed of the ducted fan

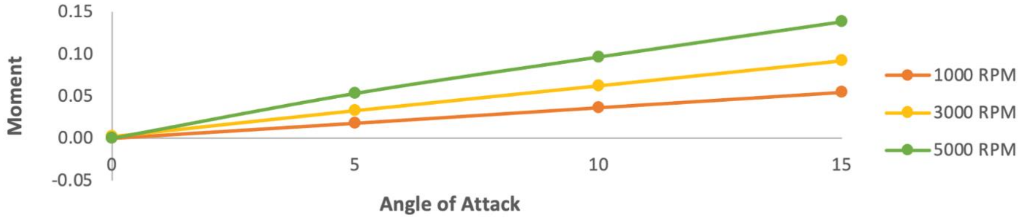

Figure 13: Moment (in Nm) versus angle of attack (in °) for flat plate's aspect ratio of 1.5 at various rotational speed of the ducted fan

From the previous figures, it is observed that there is a gradual increase in the calculated moment with increasing rotational speed of the ducted fan for a given flat plate's aspect ratio and angle of attack. For instance, in Figure 11, at angle of attack of 15°, the moment calculated is 0.13 Nm for 1000 RPM, going up to 0.18 Nm for 3000 RPM and 0.28 Nm for 5000 RPM. A similar pattern is also observed in Figure 12 and Figure 13 in the generation of moments concerning rotational speed despite the different aspect ratio of the flat plate. This finding is in line with the expectation as a higher rotational speed of the ducted fan will generate more thrust and cause a larger flow ejected behind it as well as increase the airspeed expelled onto the plate. Based on Bernoulli's principle, the pressure is low in fast air while it is high in slow air. Therefore, when the ejected airspeed increases, the speed of air over the flat plate also increases, causing the pressure above the plate to decrease. The air is moving more slowly beneath the plate and therefore, high pressure is exerted onto the plate such that it is lifted upward. This situation increases the lift force. All in all, based on the findings presented in Figure 11 to Figure 13, increasing the rotational speed of the ducted fan will generally cause the moment to increase as well, regardless of the aspect ratio of the flat plate.

### 3.3. Effects of aspect ratio of the flat plate on the moment produced

In Figure 14, the moment at angle of attack of 15° and rotational ducted fan speed of 1000 RPM for aspect ratio of 0.5 is 0.03 Nm and it decreases by 26% to 0.02 Nm as the aspect ratio is increased to 1.0. Another 17% reduction in the moment force is calculated as the aspect ratio is further increased to 1.5. On the whole, a similar trend is observed in both Figure 15 and Figure 16, which indicates that for any given angle of attack and rotational speed of the ducted fan, the value of the moment force will decrease as the aspect ratio of the flat plate is increased.

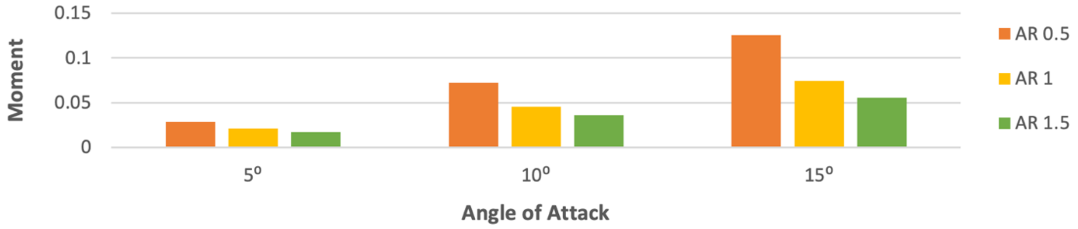

Figure 14: Moment (in Nm) versus angle of attack (in °) for rotational ducted fan speed of 1000 RPM at various aspect ratio of the flat plated

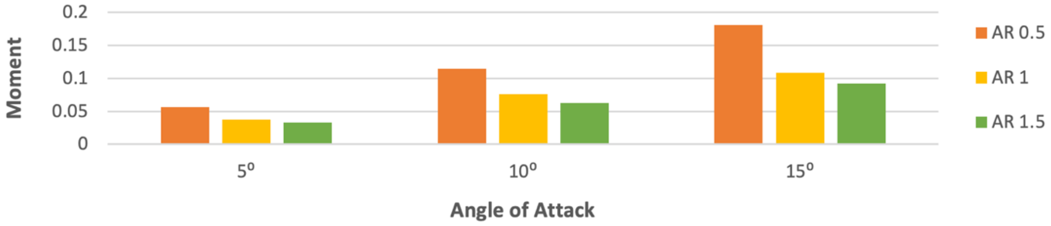

Figure 15: Moment (in Nm) versus angle of attack (in °) for rotational ducted fan speed of 3000 RPM at various aspect ratio of the flat plated

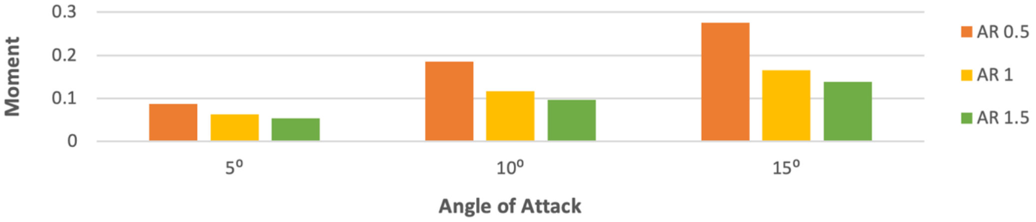

Figure 16: Moment (in Nm) versus angle of attack (in °) for rotational ducted fan speed of 5000 RPM at various aspect ratio of the flat plated

In essence, this observed trend is consistent with findings from the study by Shademan et al. [18], which reported the smaller aspect ratio prevents the flow separation from the top and bottom edges of the plate, leading to greater aerodynamic forces acting on the flat plate and may consequently cause the moment generated to become larger. Overall, regardless of the rotational speed of the ducted fan, the smallest aspect ratio of the flat plate will always give the highest moment force at any specified angle of attack. Moreover, the high moment force is also achieved when the angle of attack is higher.

All things considered, for any given angle of attack, the highest generated moment obtained in this study is for flat plate's aspect ratio of 0.5 and ducted fan's rotational speed of 5000 RPM. On the other hand, the highest pitching moment value at airspeed of 5 m/s from previous experiment is found to be 2.28 Nm when the CyFlaP is inclined at angle of attack of 20° while the lowest is 0.53 Nm at 5° angle of attack. In comparison, the highest moment value generated by the plate in this study is 0.276 Nm, which is comparatively way too low. This implies that the proposed CyFlaP design with the inclusion of the ducted fan and flat plate will not be able to resolve the longitudinal stability problem of CyFlaP. It can be deduced that the proposed use of the ducted fan and the flat plate to stabilize the CyFlaP has failed due to insufficient moment value produced. The search for better design solution to resolve the issue is therefore remains open.

## 4. Conclusion

In this research project, it is shown that the flow behind the ducted fan can facilitate the formation of lift force on the plate. The lift force generated by the plate becomes higher as the inclination angle of the plate increases from 0° to 15°. Moreover, modification on aspect ratio of the flat plate has shown that the smallest aspect ratio provides better value of moment force. Higher rotational ducted fan speed offers a greater discharged flow by the ducted fan, which consequently increases the airflow acting on the flat plate. Thus, greater aerodynamic forces are acting on the plate and hence bigger moments are produced. The maximum moment value based on the simulation result is calculated when the flat plate's aspect ratio is 0.5, angle of attack is 15° and 5000 RPM of rotating ducted fan speed. Nonetheless, by comparing the simulation results with the experimental moment produced by the CyFlaP, the lift force obtained from the ducted fan and flat plate of this control approach is found to be relatively very small. Subsequently, it produces an insufficient moment to resist the existing pitching moment on the CyFlaP. Therefore, there remains a need to finding other effective solutions to the stability issue of the CyFlaP.

## Acknowledgement

The authors acknowledge the funding for this study by the Malaysian Ministry of Education (MoE) under their Fundamental Research Grant Scheme: FRGS/1/2018/TK09/UPM/02/2 and project code 03-01-18-1950FR.

## References

[1] J. Seifert, 'A Review of the Magnus Effect in Aeronautics', Progress in Aerospace Sciences, vol. 55, pp. 17-45, 2012.

[2] W. Swanson, 'The Magnus Effect: A Summary of Investigations to Date', Journal of Basic Engineering, vol. 83, no. 3, pp. 461-470, 1961.

[3] A. Lafay, 'Sur l'inversion du phenomène de Magnus', Comptes Rendus Hebdomadaires des Séances de l'Académie des Sciences, vol. 151, pp. 867-868, 1910.

[4] J. Borg, 'Magnus Effect: An Overview of Its Past and Future Practical Applications', NASA STI/Recon Technical Report N, vol. 86, p. 30102, 1986.

[5] J. Monteiro, J. C. Pascoa and C. Xisto, 'Analytical Modeling of a Cyclorotor in Forward Flight', SAE Technical Paper, 0148-7191, 2013.

[6] M. Schwaiger and D. Wills, "D-Dalus VTOL–Efficiency Increase in Forward Flight', Aircraft Engineering and Aerospace Technology, vol. 88, no. 5, pp. 594-604, 2016.

[7] M. S. I. Roslan, 'Rotational Speed Analysis on Double Rotating Cylinder For High Altitude Platform Station (HAPS)', Bachelor Thesis, Universiti Putra Malaysia, 2021.

[8] M. M. Noor, 'Computational Analysis of Pitching Moment On High Altitude Platform (HAPS) using Computational Fluid Dynamics', Bachelor Thesis, Universiti Putra Malaysia, 2021.

[9] J. Anderson, Fundamentals of Aerodynamics, McGraw Hill, 2011.

[10] L. Cho, S. Lee and J. Cho, 'Numerical and Experimental Analyses of the Ducted Fan for the Small VTOL UAV Propulsion', Transactions of the Japan Society for Aeronautical and Space Sciences, vol. 56, no. 6, pp. 328-336, 2013.

[11] A. Mgaidi, A. S. M. Rafie, K. Ahmad, R. Zahari, M. F. A. Hamid and O. F. Marzuki, 'Numerical and Experimental Analyses of the Flow Around a Rotating Circular Cylinder at Subcritical Regime of Reynolds Number using k-ε and k-ω-sst Turbulent Models', ARPN Journal of Engineering and Applied Sciences, vol. 13, no. 3, pp. 954-961, 2006.

[12] F. R. Menter, 'Two-Equation Eddy-Viscosity Turbulence Model for Engineering Applications', AIAA Journal, vol. 32, no. 8, pp. 1598-1605, 1994.

[13] D. C. Wilcox, 'Reassessment of the Scale-Determining Equation for Advanced Turbulence Models', AIAA Journal, vol. 26, no. 11, pp. 1299-1310, 1988.

[14] H. M. Ali, A. S. M. Rafie and S. A. M. Ali, 'Numerical Analysis of Leading Edge Cylinder Aerofoil on Selig S1223 for Moving Surface Boundary Control," Journal of Aeronautics, Astronautics and Aviation, vol. 53, no. 2, pp. 143-154, 2021.

[15] H. M. Ali, A. S. M. Rafie, S. A. M. Ali and E. Gires, "Computational Analysis of the Rotating Cylinder Embedment onto Flat Plate," CFD Letters, vol. 13, no. 12, pp. 133-149, 2021.

[16] H. M. Ali, A. S. M. Rafie, M. F. A. Hamid and S. A. M. Ali, "Comparative Computational Study of Double Rotating Cylinder Embedded on Selig S1223 Aerofoil and Flat Plate for High Altitude Platform," Pertanika Journal of Science & Technology, vol. 30, no. 4, pp. 2767-2788, 2022.

[17] H. Heisler, Advanced Vehicle Technology, Vitalsource Technologies, Inc., 2002.

[18] M. Shademan and A. Naghib-Lahouti, 'Effects of Aspect Ratio and Inclination Angle on Aerodynamic Loads of a Flat Plate', Advances in Aerodynamics, vol. 2, no. 1, pp. 1-23, 2020.

# COMPUTATIONAL AERODYNAMICS ANALYSIS OF A BLUFF BODY WITH ROTATING CYLINDER AS DRAG REDUCER

**Muhammad Irfan Kamid [1], Hidayatullah Mohammad Ali [1, *] and Azmin Shakrine Mohd Rafie [1]**

1. Department of Aerospace Engineering, Faculty of Engineering, Universiti Putra Malaysia, 43400 Serdang, Selangor, Malaysia

*Correspondence: hidayatmaddali@gmail.com

**Abstract:** This study is aimed to address the issue of dangerous emissions into the environment by the operation of large container lorries. These big vehicles use much of their engine power to overcome the aerodynamic drag due to their movement, which also means a lot of fuel is being burned in this process. To reduce the fuel consumption, hence the gas emissions, the aerodynamic efficiency of the vehicle can be improved through its design. Based on this notion, the main objective of this work is to analyse the impacts from the use of a rotating cylinder as a drag reducer for heavy-duty vehicles. The incorporation of the rotating cylinder is expected to be able to reduce the drag forces acting on the vehicles and also increase their design aerodynamic efficiency. For this study, a container lorry is modelled and analysed using the computational simulation software, ANSYS with several different placements of the rotating cylinder around the lorry as its drag reducers. The obtained results indicate that the use of the cylinder can reduce drag by as much as 36% in comparison to the baseline design of the container lorry without rotating cylinder. It is observed that the cylinder helps to lessen the airflow circulating at the back and top of the container lorry, subsequently lower its drag coefficient. All in all, the findings from this study demonstrate the potential of using rotating cylinders as drag reducers to solve the issue of gas emissions from container lorries.

**Keywords:** ANSYS; aerodynamics analysis; bluff body; rotating cylinder; drag reducer

## 1. Introduction

Bluff bodies have been scientifically studied with regard to their aerodynamic characteristics and it is of particular interest to establish their drag performance with blunt bases. Designs of bluff bodies can be related to large road vehicles and their studies help to better understand the vehicles' aerodynamics. For instance, for a typical Class 8 line-haul tractor-trailer vehicle running at highway speeds, its resultant aerodynamic drag will cause considerable parasitic loss. In fact, a typical heavy truck vehicle uses around 65% of its entire energy at a speed of 70 mph to overcome aerodynamic drag [1]. Over the last decades, due in part by increase in fuel prices and also environmental concerns, researchers have made significant advancement in understanding the mechanisms for drag reduction with blunt-based bluff bodies [2]. In conjunction to this, aerodynamic performance has been considered in many road vehicle designs, which leads to mostly tapered design shapes to minimize the drag pressure. However, for heavy road vehicles such as container lorries, this entails significant design changes that could undesirably compromise their cargo capacity. Therefore, instead of changing the overall vehicle designs, it can be observed that some add-on features are applied to the existing heavy road vehicle designs to help improve their aerodynamic performance. In this case, aerodynamically-designed add-on parts are attached to the front as well as the other parts of the heavy road vehicle, which will adjust the effective form or shape of the vehicle to be more streamlined without altering its projected frontal area. Due to their exterior forms, sizes and also positions, the external attachments can reduce the aerodynamic drag of the heavy road vehicles [3]. As a result, the reduced aerodynamic drag will improve the vehicle's fuel economy and lower its greenhouse gas emissions [4]–[7].

Thus far, the aerodynamic effects of many existing models of aerodynamic fairings (front and side) and their configurations have not been thoroughly researched or documented. Base drag is one of the key contributions to aerodynamic drag, which is the factor that determines fuel consumption. According to prior research, the base drag occurs in the back end of the vehicle. For the heavy road vehicles such as the container lorries, this is where the cargo area is located. A bluff body vehicle traveling at constant speed on a flat level road will spend up to 40% of its fuel energy to counteract its aerodynamic drag and 45% to overcome its rolling resistance, leaving just 15% to drive the gear and losses [8]. Several methods have been applied to improve the aerodynamics of the vehicles including passive and active flow control methods. From previous conducted study, 4% improvement has been achieved by curving the back of the vehicle, 3% improvement with nose cone and 7% improvement with chassis skirt [9]. Furthermore, for commercial vehicles, the coefficient of drag, $C_d$ falls as the windshield attack angle is increased [9]. In the meantime, a device has been patented for vehicles as illustrated in Figure 1, which features resilient prongs along the rear edge of the vehicle body, extending beyond the edge in a flow-wise direction [10]. The function of this device is to improve the aerodynamic performance by reducing the drag caused by airflow over the vehicle's rear edge. Each prong is separated from the next, and flexible enough to deflect above and below the first plane defined by the vehicle's surface under the impact of the airflow over the vehicle at a certain speed. The prongs may have a composite structure or incorporate a vulcanized rubber substance, with uniform or tapering cross-section and radial corners. These prongs can be repositioned from a deployed position to a retracted position, either manually or by attaching the device to a rotating frame member that can be rotated between the two positions. On the other hand, conducted study on a 1/6 model truck and trailer has shown improved aerodynamics by 12.5% and 28% through installation of vertical and horizontal spoilers on the vehicle's front, respectively [11]. Moreover, other exemplary improvement methods include the use of redirector plates [12] and flow deflectors [13]. However, it can be deduced that most of these body alterations are rather substantial and therefore rather unsuitable for the current container lorry designs as their cargo capacity may need to be sacrificed.

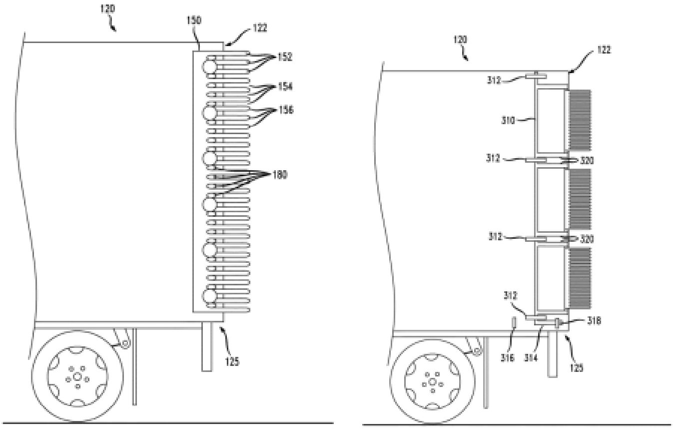

Figure 1: Aerodynamic drag reduction device [10]

Alternatively, it is believed that rotating cylinders have a good potential to be used as drag reducers for heavy road vehicles including container lorries. According to a conducted study, such devices could help to disrupt the airflow over and around the moving vehicle when they are installed on the front and back of the container or vehicle [14]. The rear spoiler is usually used to distribute the air, which lessens the turbulence that the moving vehicle creates, and subsequently aids in reducing air drag and turbulent flow. On the other hand, a wind tunnel test for installation of rotating cylinder on a container lorry has been conducted and the obtained results indicate promising improvement in drag reduction [15]. Based on this notion, this study is aimed to investigate the aerodynamic effects from use of rotating cylinders as drag reducers for a container lorry that is considered as bluff body using computational fluid dynamics (CFD) method. The CFD simulation analysis in this study is done with ANSYS software tool.

## 2. Methodology

### 2.1. Pre-processing

ANSYS is a widely used CFD tool for simulating and analysing fluid flow and related phenomena. It utilises finite volume method (FVM) to discretise the governing equations, allowing for visualization and post-processing tasks. Known for its accuracy and user-friendliness, ANSYS is a widely applied tool for designing and optimising products and processes in various industries like aerospace, automotive, chemical and civil engineering. A mathematical model, consisting of equations and boundary conditions, is necessary for the numerical approach. FVM and $k$-epsilon model are used to solve the Navier-Stokes equations for two-dimensional Cartesian coordinates. The pre-processor, which essentially serves as the link between the user and the solver, provides a user-friendly interface and converts input for the solver.

For this study, the design of the 2D model of the container lorry is set with the dimension as listed in Table 1. In the previous conducted experimental work [15], the rotating cylinder is placed at the front of the container as indicated in Figure 2. The first placement of the cylinder is initially positioned at 215 mm as measured from the bottom of the container. On the other hand, the second and third considered placements of the cylinder are positioned at 16 mm and 32 mm below the first placement, respectively. As also illustrated in Figure 2, the computational analysis in this study also considers three new potential placements of the rotating cylinder at the back of the container. The first new placement is at the top back of the container. The second new considered placement is at the back rear corner of the container, which is 215 mm as measured from the bottom of the container. Last but not least, the third positioning of the rotating cylinder is at the rear top of the container, which is 50 mm higher than the new second positioning and 50 mm aft at the same height of the first new position.

As for the computational domain, a fluid volume of air has been created surrounding the vehicle in order to simulate the air movement around it. It should be noted that the dimensions of the domain are set to 3 m × 1.5 m (length × height) to match the average size of the wind tunnel used in the previous experimental setup. This will enable a direct validation study to be conducted through the comparison of results from the CFD simulation and the previous experimental work for the three initial positioning considered for the rotating cylinders on the container lorry. Figure 3 depicts the geometric modeling of the container lorry (clean design without the rotating cylinder) and the domain after their construction.

Table 1: Parameters of the container lorry model

| Parameter | Value |
|---|---|
| Container's Height | 0.240 m |
| Trailer's Height | 0.180 m |
| Total Length | 0.890 m |
| Container's Length | 0.600 m |
| Trailer's Length | 0.200 m |
| Cylinder's Radius | 0.022 m |

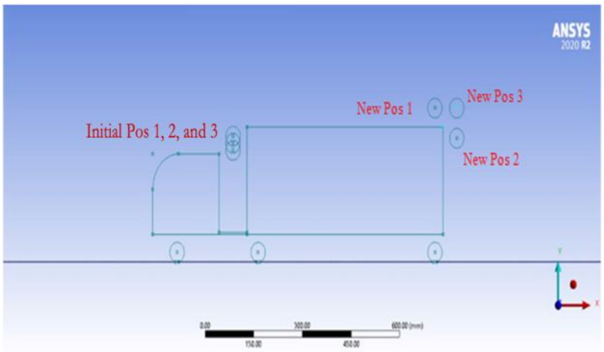

Figure 2: Illustration of the container lorry with considered positioning of rotating cylinder

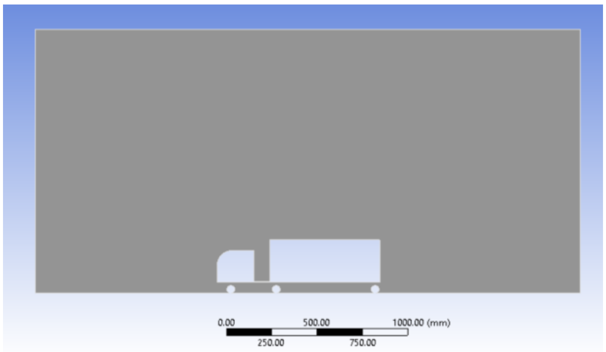

Figure 3: Computational analysis model of the container lorry with no rotating cylinder

Furthermore, grid generation is a crucial part of the CFD simulation process since it influences not only the simulation duration but also the accuracy of the results. In short, this refers to the creation of a mesh or grid that is associated with a domain and its boundaries. Edge sizing is used for the setting of the model where all of the meshes use 200 divisions on every edge. To achieve satisfactory results, it is recommended that the inflation parameters of a maximum of 10 layers and a growth rate of 1.2 are set on the surfaces of each model [16]-[18]. It should be noted that it has been discovered that the accuracy of computational results can be improved by using a small number of mesh elements [19]. The inflation layer is one of the important factors that affect the accuracy of CFD simulations. If the number of layers is insufficient, the simulation results will not be accurate. Meanwhile, when it is too large, the simulation time will increase. This supports the importance of selecting appropriate inflation parameters to achieve satisfactory CFD simulation results.

The detailed information on mesh settings and boundary conditions for this study are tabulated in Table 2 and the generated grid around the container lorry model is illustrated in Figure 4. As observed in Figure 4, named selection setting is used to name every boundary: inlet as 'velocity-inlet' ranging from 0 m/s to 32 m/s, road as 'ground', top wall as 'symmetry', whole container lorry as 'body', cylinder as 'cylinder' with 'no slip' condition and 'rotational' moving wall, and the outlet as 'pressure-outlet' where its pressure is set to constant and equals to the atmospheric pressure.

Table 2: The mesh setting for this study

| **Mesh Specification** | |
|---|---|
| Growth Rate | 1.2 |
| De-feature Size | 3.5e-004 m |
| Curvature Minimum Size | 7.0e-004 m |
| Curvature Normal Angle | 18.0 ° |
| Smoothing | High |
| Skewness | 0.18227 |
| Orthogonal Quality | 0.95941 |
| **Inflation Specification** | |
| Smoothing | High |
| Inflation Option | First Layer Thickness |
| First Layer Height | 0.1 mm |
| Maximum Layers | 10 |
| Growth Rate | 1.2 |

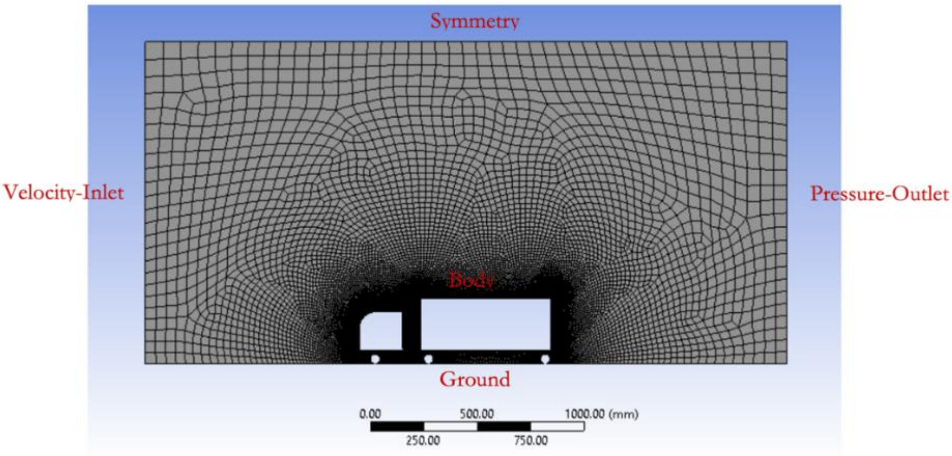

Figure 4: Finished meshed model

In the meantime, the essential mesh metrics with regards to its skewness and orthogonal quality are tabulated in Table 3. The average skewness quality of the mesh metrics is found as 0.18227 whereas the average orthogonal quality is 0.95941. In general, highly skewed cells might make the solution unstable and impede the accuracy of the results. On the whole, these metrics for the skewness and orthogonal quality obtained can be taken to be excellent as indicated by the standard quality spectrum in Ref. [20].

Table 3: Skewness and orthogonal quality mesh metrics

| **Mesh Metrics** | **Skewness** | **Orthogonal Quality** |
|---|---|---|
| Minimum | 0.00106 | 0.42732 |
| Maximum | 0.68227 | 1.00000 |
| Average | 0.18227 | 0.95941 |
| Standard Deviation | 0.10919 | 0.04560 |

### 2.2. Solver

Before conducting the computational analysis, the capability of the CFD solver must be equipped with the pertinent settings for the desired condition. In this case of a rotating cylinder, the velocity and also the position of the cylinder change over time, so a transient analysis is needed to accurately capture the behaviour of the system. With this in mind, a pressure-based transient-state solution is applied for this analysis. The time step size should be small enough to capture the rapid changes in the system but not too small such that the simulation becomes computationally expensive or numerically unstable. The required number of time steps depends on the duration of the simulation and the size of the time step. Table 4 shows the list of the problem-solving techniques and input data.

Calculations are performed on computers utilizing an iterative process where the precision of the result increases with each iteration. In general, $k$-epsilon ($k$-$\varepsilon$) model is one of the most common mean flow characteristics for turbulent flow conditions in ANSYS computation, which belongs to Reynolds Averaged Navier-Stokes (RANS) family of turbulence models. The model solves two equations: one for the turbulent kinetic energy, $k$ and another for the rate of dissipation of turbulence, $\varepsilon$. These equations allow for the prediction of turbulence characteristics of the flow field. In this two-equation model, the turbulent characteristics of the flow are represented by two additional transport equations. As a result, a two-equation model may take historical influences like convection and turbulent energy diffusion into consideration. Several previous studies have used $k$-$\varepsilon$ model to simulate the aerodynamics of heavy road vehicles similar to the container lorry in this study. For example, $k$-$\varepsilon$ model was used in a study to analyse aerodynamic characteristics of a heavy-duty truck [14]. In that study, it has been found that the primary methods for enhancing aerodynamic properties of heavy-duty commercial trucks are by using *k-ε* model and reducing the vortex at the cab and container as well as at the container's end and bottom.

Table 4: The solver setting for this study

| **General** | |
|---|---|
| Type | Pressure Based |
| Velocity Formation | Absolute |
| Time | Transient |
| 2D Space | Planar |
| Time Step Size | 0.01 |
| Number of Time Steps | 100 |
| **Model** | |
| Viscous | Realizable *k-ε* |
| Wall Functions | Non-equilibrium |
| **Reference Values** | |
| Velocity | 0 – 32 m/s |
| Cylinder Rotation | 1) 0 RPM (static)<br>2) 3000 RPM or 314.159265 rad/s (rotating) |
| Reference Area | 0.24 m × 0.89 m = 0.214 m$^2$ |
| 2D Space | Planar |

There are three versions of the *k-ε* model, which are the standard, Re-Normalisation Group (RNG) and realizable *k-ε* models. The turbulence kinetic energy and dissipation rate equation for these standard, RNG and realizable *k-ε* models are presented by the following equations. Firstly, both Equation 1 and Equation 2 are the transport equations for the standard *k-ε* model.

$$\frac{\partial}{\partial t}(\rho k) + \frac{\partial}{\partial x_i}(\rho k u_i) = \frac{\partial}{\partial x_j}\left[\left(\mu + \frac{\mu_t}{\sigma_k}\right)\frac{\partial k}{\partial x_j}\right] + G_k + G_b - \rho\epsilon - Y_M + S_k \tag{1}$$

$$\frac{\partial}{\partial t}(\rho\epsilon) + \frac{\partial}{\partial x_i}(\rho\epsilon \mathrm{u_i}) = \frac{\partial}{\partial x_j}\left[\left(\mu + \frac{\mu_t}{\sigma_\epsilon}\right)\frac{\partial \epsilon}{\partial x_j}\right] + C_{1\epsilon}\frac{\epsilon}{k}(G_k + \mathrm{C_{3\epsilon}G_b}) - C_{2\epsilon}\rho\frac{\epsilon^2}{k} + S_\epsilon \tag{2}$$

On the other hand, both Equation 3 and Equation 4 are the transport equations for the RNG *k-ε* model.

$$\frac{\partial}{\partial t}(\rho k) + \frac{\partial}{\partial x_i}(\rho k u_i) = \frac{\partial}{\partial x_j}\left[\alpha_k \mu_{eff}\frac{\partial k}{\partial x_j}\right] + G_k + G_b - \rho\epsilon - Y_M + S_k \tag{3}$$

$$\frac{\partial}{\partial t}(\rho\epsilon) + \frac{\partial}{\partial x_i}(\rho\epsilon \mathrm{u_i}) = \frac{\partial}{\partial x_j}\left[\alpha_\epsilon \mu_{eff}\frac{\partial \epsilon}{\partial x_j}\right] + C_{1\epsilon}\frac{\epsilon}{k}(G_k + \mathrm{C_{3\epsilon}G_b}) - C_{2\epsilon}\rho\frac{\epsilon^2}{k} - \mathrm{R_\epsilon} + S_\epsilon \tag{4}$$

Finally, both Equation 5 and Equation 6 are the transport equations for the realizable *k-ε* model.

$$\frac{\partial}{\partial t}(\rho k) + \frac{\partial}{\partial x_j}(\rho k u_j) = \frac{\partial}{\partial x_j}\left[\left(\mu + \frac{\mu_t}{\sigma_k}\right)\frac{\partial k}{\partial x_j}\right] + G_k + G_b - \rho\epsilon - Y_M + S_k \tag{5}$$

$$\frac{\partial}{\partial t}(\rho\epsilon) + \frac{\partial}{\partial x_j}(\rho\epsilon \mathrm{u}_j) = \frac{\partial}{\partial x_j}\left[\left(\mu + \frac{\mu_t}{\sigma_\epsilon}\right)\frac{\partial \epsilon}{\partial x_j}\right] + \rho\mathrm{C_1}S\epsilon - \rho C_2\frac{\epsilon^2}{k + \sqrt{v\epsilon}} + \mathrm{C_{1\epsilon}}\frac{\epsilon}{k}\mathrm{C_{3\epsilon}G_b} + S_\epsilon \tag{6}$$

In the above equations, $G_k$ stands for the creation of turbulence kinetic energy owing to the mean velocity gradients while $G_b$ is the generation of turbulence kinetic energy due to buoyancy. Furthermore, $Y_M$ is the variable dilatation in compressible turbulence's contribution to total dissipation rate, $\alpha_k$ is the inverse effective Prandtl number for $k$, $\alpha_\varepsilon$ is the inverse effective Prandtl number for $\varepsilon$, $\sigma_k$ is turbulent Prandtl value for $k$, $\sigma_\varepsilon$ is turbulent Prandtl value for $\varepsilon$, $\varrho$ is fluid density, $u$ is fluid velocity, $x_i$ and $x_j$ are the Cartesian coordinate direction, $\varepsilon$ is turbulence dissipation rate, $\mu$ is the fluid dynamic viscosity, and $\mu_t$ is the turbulent viscosity. Last but not the least, $C_{1\varepsilon}$, $C_2$, $C_{2\varepsilon}$ and $C_{3\varepsilon}$ are constants while $S_k$ and $S_\varepsilon$ are user-defined source terms.

Generally, the $k$-$\varepsilon$ turbulence model might not be effective in predicting turbulence flow in certain situations, particularly when there are unfavourable pressure gradients present. This is mainly because the $k$-$\varepsilon$ model assumes that the turbulent stresses are proportional to the mean flow gradient, which may not be accurate in cases where the pressure gradient is high [21]. Researchers have shown that in cases of strong adverse pressure gradients, $k$-$\varepsilon$ model can lead to erroneous predictions and may not accurately capture the flow behaviour [22]. It can be noted that the RNG $k$-$\varepsilon$ model is the modified version of the standard $k$-$\varepsilon$ model, which includes added model constants and terms to further improve the accuracy of the predictions. Meanwhile, the $k$ equation for the realizable $k$-$\varepsilon$ model is similar to the standard $k$-$\varepsilon$ model with the added constants but the $\varepsilon$ equation is notably different between the two $k$-$\varepsilon$ models. As can be observed in Equation 6, it is interesting to note that it does not have the same $G_k$ term as other $k$-$\varepsilon$ models as it does not involve the production of $k$. In essence, this current form is thought to depict the transmission of spectral energy more accurately. The destruction term, which is the last term on the right side of Equation 6, does not have any singularities and this indicates that even if $k$ disappears or shrinks to zero, its denominator will never do. This is a much desirable feature and stands in contrast to conventional $k$-$\varepsilon$ models, which exhibit a singularity because $k$ is present in the denominator. Due to this feature, realizable $k$-$\varepsilon$ model is used to overcome the well-known shortcomings of the conventional $k$-$\varepsilon$ model. With the use of this model, it is feasible to obtain satisfactory results for integral values such as the drag coefficient that are more accurate, converge rapidly and quite stable.

## 2.3. Validation study for solver accuracy

To evaluate the accuracy of the findings produced by using the aforementioned solver parameters, initial test case of the baseline container lorry design model without any rotating cylinder is conducted. The simulated relative inlet airspeed for this test case is between 0 m/s to 31.5 m/s. The results obtained from the simulation analysis are compared with the published experimental results in Ref. [15], which is shown in Figure 5. It can be observed that the drag coefficient, $C_d$ obtained from the simulation analysis is closely similar to the one obtained from the wind tunnel experiment. The value difference is less than 10%, which is taken to be within acceptable range of accuracy for Reynolds number, Re ranging between 0 to 600,000. All in all, the solver parameters are taken to be appropriate to be for this analysis study.

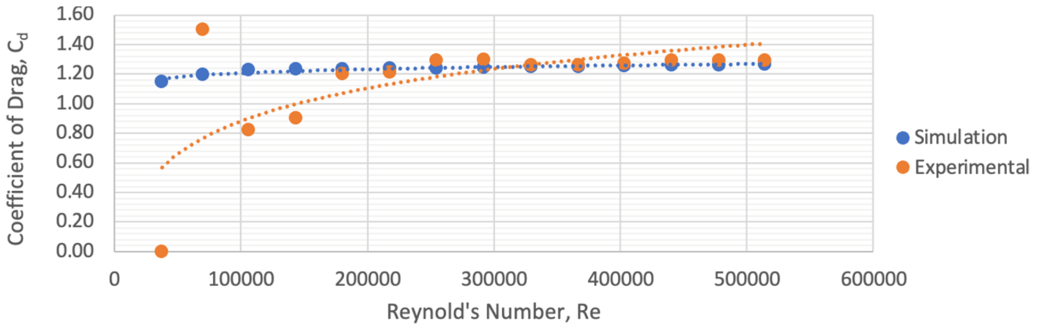

Figure 5: $C_d$ vs Re obtained from the validation study

## 3. Results and Discussion

There are three control variables that are varied in the CFD simulation analysis for this study. The first one is the velocity of the air entering the inlet, which is varied between 0 m/s to 32 m/s to control and manipulate Re around the airflow of the truck. The second variable is the rotation of the cylinder, where is set for two conditions: static and moving (rotating). The rotational speed of the cylinders is set to 3000 RPM for the simulated moving condition. Finally, the last variable is the position of the cylinder as indicated in previous Figure 2.

### 3.1. Comparison with experimental results for three initial positions of the cylinder

The results of previous validation study in Figure 5 are taken as the baseline reference. To compare with the previous experimental results as published in Ref. [15], the simulation analysis is conducted for the three initial positions of the rotating cylinder as illustrated in previous Figure 2. Figure 6 shows the previous experimental results while Figure 7 depicts the results of CFD simulation analysis in this study.

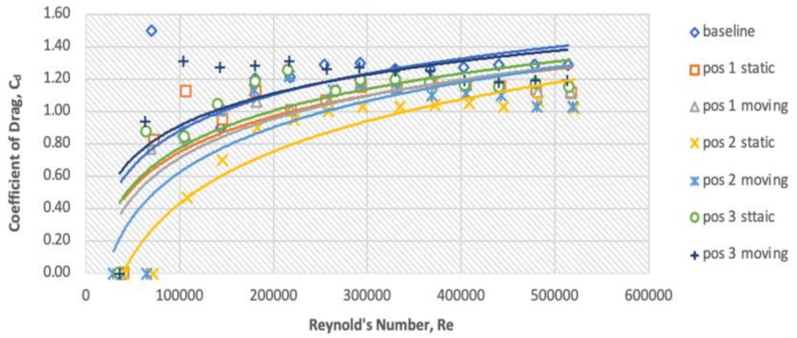

Figure 6: Experimental results of $C_d$ vs Re for three initial positioning

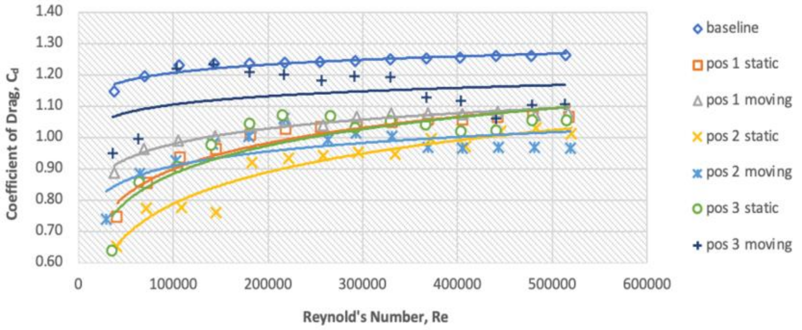

Figure 7: Simulation results of $C_d$ vs Re for three initial positioning

For the first positioning of rotating cylinder, it can be observed that simulation result is more stable and steadier with increasing Re in comparison to experimental data where it fluctuates back and forth in the first few takes before becoming more stable toward higher Re. Average differences of 7.05% and 7.85% are respectively recorded between the results of the simulation and the experiment for static and moving conditions at this first initial position. It can be observed that the static cylinder performed more efficiently as compared to the moving cylinder, which is reflected by the lower average $C_d$ for the static cylinder than that of the moving cylinder. Nonetheless, note that this difference is just significant at low Re and as Re increases, the values of $C_d$ converges to around the same values for both static and moving cylinder conditions. This observation trend is true for both simulation and experimental results. Similar observation can also be seen for the second initial positioning of the cylinders. In this case, the average differences between the simulation and the experimental results are 9.70% and 9.89% for the static and moving configurations of the cylinders, respectively. The results from simulation analysis are more stable and steadier. Moreover, at this positioning, the static cylinder has again performed more effectively than the moving cylinder. The noted differences between them are significantly visible at low Re but diminish as Re increases. On the other hand, for the third considered initial positioning of the cylinder, average differences between simulation and experimental results for both static and moving configurations of the cylinders are 9.68% and 6.70%, respectively. Based on previous Figure 6 and Figure 7, it is noticeable that values of $C_d$ for both static and moving cylinder configurations increase at low Re up until it reaches 200,000 where it began to slowly decrease. For Re higher than 200,000, $C_d$ has minor fluctuations and inconsistencies, and shows a visible trend between the static and moving cylinder configurations. Static cylinder configuration is shown to achieve a much better drag reduction than the moving configuration. This could be attributed to the RPM incompatibility with relative free stream velocity that has caused more turbulence in the air and affected the drag of the container lorry.

Overall, for these three initial considered positioning of the rotating cylinder, both simulation and experimental results show that the static second position corresponds to the lowest value of $C_d$, which is about 25.50% reduction compared to the other considered configurations. It is also good to note that the moving cylinder configuration at each position has higher drag compared to the static configuration. This could be because the chosen RPM is not optimal for velocity of free stream air and positioning of the cylinder used in this study. Nonetheless, the moving cylinder configurations still perform better than the baseline container lorry model

## 3.2. Simulation results for three new positions of the cylinder

Figure 8 shows the simulation results for the first new considered positioning of rotating cylinder on the container lorry model. It can be observed, unlike the result for previous initial positioning of the cylinder, the trend of $C_d$ appears to bend downward. As Re increases, the value of $C_d$ for both static and moving cylinder configurations significantly reduces up until Re of 300,000. Although the static cylinder configuration initially performs better than the moving cylinder configuration, its corresponding value of $C_d$ starts to increase and ultimately converge with that of the moving cylinder configuration when Re is above 300,000. All in all, implementation of the static and moving rotating cylinder is shown to reduce the $C_d$ of the container lorry by averagely 18.74% and 18.5%, respectively.

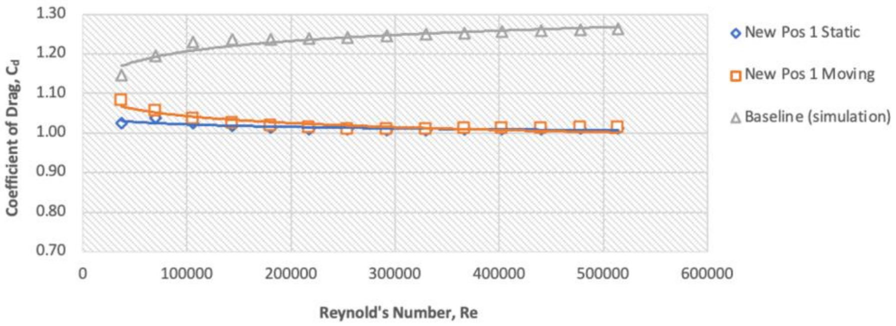

Figure 8: Simulation results of $C_d$ vs Re for first new position

A similar trend is also essentially observed for the second new positioning of the rotating cylinder as depicted in Figure 9. Values of $C_d$ for both static and moving cylinder configurations decrease with increasing Re up until about 300,000. After that point, values of $C_d$ seem to have converged and maintain at the same value with increasing Re. In similar fashion, despite drag performance of the static cylinder configuration is better at lower Re, the values of $C_d$ for both static and moving cylinder configurations ultimately converge to a similar value at high Re. In terms of comparison with the drag performance for the baseline container lorry, implementing the static and moving cylinder configurations can reduce the value of $C_d$ by 36.0% and 35.8% on average, respectively. As presented in Figure 10, an essentially similar trend to Figure 9 is observed for the drag performance of the static and moving cylinder configurations at the third new positioning. At this considered new third position, average drag reduction of 26.2% and 25.7% has been obtained by implementing the static and moving cylinder configurations, respectively, as compared to that for the baseline container lorry design model.

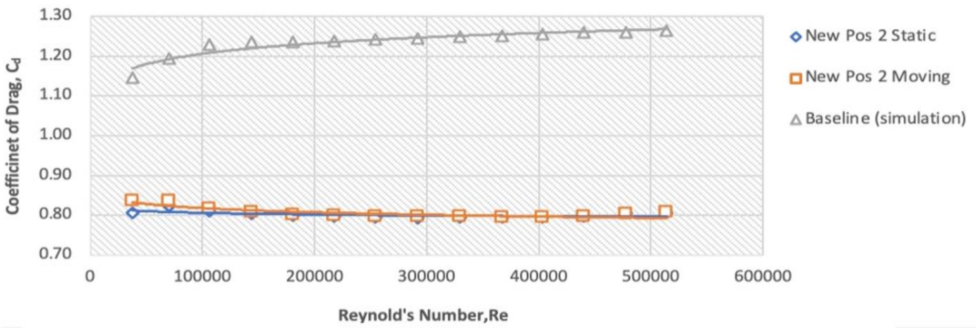

Figure 9: Simulation results of $C_d$ vs Re for second new position

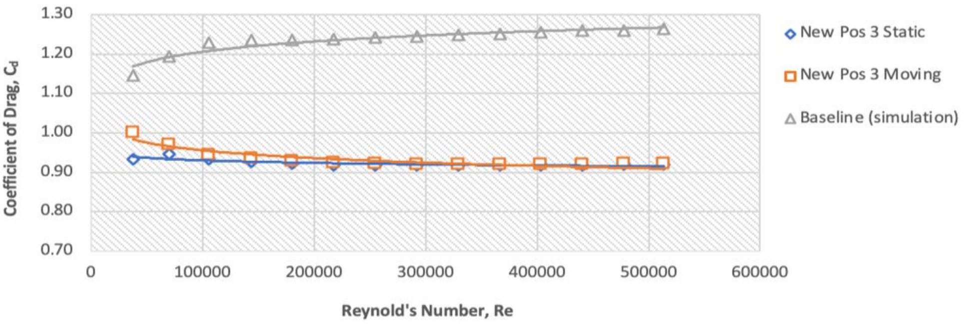

Figure 10: Simulation results of $C_d$ vs Re for third new position

On the whole, it is clearly seen from the obtained simulation results that the new second positioning of the rotating cylinder has the best drag performance. This can be contributed to the reduction of the drag on the container lorry as it helps to diminish the turbulence that is created when the vehicle moves. At the rear of the container lorry, with this placement of the rotating cylinder, it will disrupt and disperse the air around it, which reduces the created air turbulence and subsequently lessens the drag. Figure 11 illustrates the velocity streamlines where recirculation or swirling of airflow at the rear of the container lorry by placing the rotating cylinder at the considered new second position. It should also be noted that this positioning of rotating cylinder on the container lorry performs much better than any of the three initial positions discussed in previous section.

Moreover, the observed independence of $C_d$ towards Re beyond the certain limit is believed to be likely due to the formation of a fully turbulent boundary layer over the surface of the object, which leads to relatively constant level of skin friction drag. This notion is supported by several previous researches. For instance, a study found that $C_d$ of a sphere became independent of Re when it reached the critical Re value of $3.5 \times 10^5$, which corresponds to the condition for the onset of fully turbulent boundary layer flow [23]. In this case, the transition from laminar to turbulent in the boundary layer around the sphere is what causes the higher momentum at the boundary and the delay in the flow separation [24]. It should be noted that the value of Re at which the $C_d$ becomes independent may depend on various factors such as the shape and surface roughness of the object, as well as the flow conditions. Further research needs to be conducted to investigate the exact mechanism behind this phenomenon and determine the specific conditions in which it will occur for different objects.

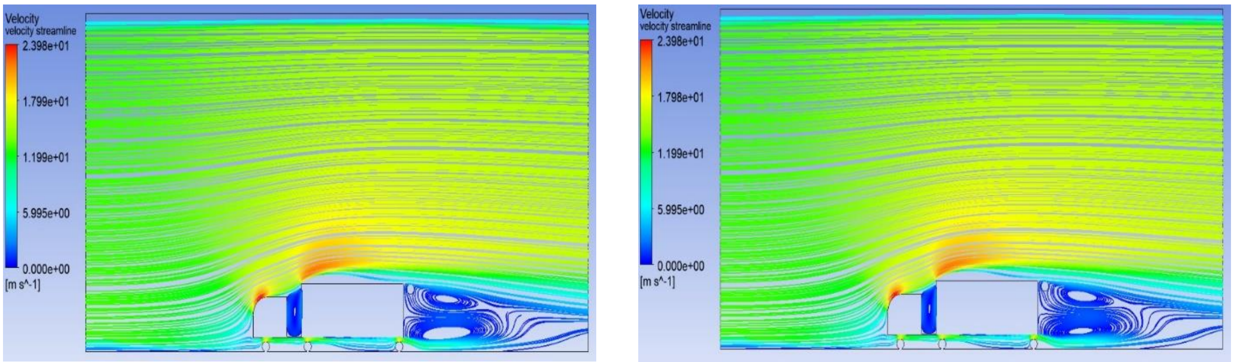

(a) Static cylinder configuration (b) Moving cylinder configuration

Figure 11: Velocity streamlines of container lorry with new second positioning of rotating cylinder

## 4. Conclusion

This research work explores the possible effects of using rotating cylinder as drag reducers on the container lorry design. In total, six different positions of the rotating cylinder on the container lorry are considered, with two modes of static and moving configurations at each position. The CFD simulation analysis is carried out for this study using the ANSYS software. All in all, based on the results, it can be concluded that the use of rotating cylinder has a good potential to reduce the drag on the container lorry when it moves on the road. Of all the six considered positioning, the new second position of the rotating cylinder is shown to have the best drag performance, which corresponds to about 36.0% reduction in drag compared to that of the clean baseline design of the container lorry without any rotating cylinder. In addition, the static cylinder configuration outperforms the moving cylinder configuration at each of the considered positions. This situation can be contributed to the less than ideal setting of the RPM for the moving cylinder with respect to the settings of free-stream air velocity and cylinder location. For the future work, the design of the rotating cylinder can be enhanced. In this simulation study, the cylinder is designed as a plain cylinder shape. Various other cylinder designs can be explored to study the effects of its shape on the drag performance of the heavy road vehicles. Furthermore, the analysis on the cost-efficiency of implementing this drag reducing mechanism can also be done.

## Acknowledgement

The authors acknowledge the funding of this research from Ministry of Education Malaysia through their Fundamental Research Grant Scheme: FRGS/1/2018/TK09/UPM/02/2 (Project Code: 03-01-18-1950FR).

## References

[1] R. McCallen, R. Couch, J. Hsu, F. Browand, M. Hammache, A. Leonard, M. Brady, K. Salari, W. Rutledge, J. Ross, B. Storms, J. T. Heineck, D. Driver, J. Bell, and G. Zilliac, 'Progress in Reducing Aerodynamic Drag for Higher Efficiency of Heavy Duty Trucks (Class 7-8)', SAE Technical Paper Series, 1999-01-2238, 1999.

[2] S. Balkanyi, L. Bernal, B. Khalighi, and V. Sumantran, 'Dynamics of Manipulated Bluff Body Wakes', Fluids 2000 Conference and Exhibit, Denver, USA, 19-22 June, 2000.

[3] H. Chowdhury, H. Moria, A. Ali, I. Khan, F. Alam, and S. Watkins, ‘A Study on Aerodynamic Drag of a Semi-Trailer Truck’, Procedia Engineering, vol. 56, pp. 201-205, 2013.

[4] R. Snyder, ‘Tire Rolling Losses and Fuel Economy’, SAE Special Publication, 74, 1997.

[5] H. Chowdhury, B. Loganathan, I. Mustary, H. Moria, and F. Alam, ‘Effect of Various Deflectors on Drag Reduction for Trucks’, Energy Procedia, vol. 110, pp. 561-566, 2017.

[6] D. Landman, R. Wood, and W. Seay, ‘Understanding Practical Heavy Truck Drag Reduction Limits’, SAE Publication, 2009-01-2890, 2009.

[7] R. E. Schoon, ‘On-road Evaluation of Devices to Reduce Heavy Truck Aerodynamic Drag’, SAE Technical Paper, 0148-7191, 2007.

[8] J. Christensen, K. P. Glaeser, T. Shelton, B. Moore, and L. Aarts, "Innovation in Truck Technologies," OECD/ITF Joint Transport Research Centre Discussion Paper, 2010.

[9] M. F. Sari, ‘The Aerodynamic Analysis of Air Resistance Affecting the Front Form of Light Commercial Vehicles and Its Effect on Fuel Consumption’, Master Thesis, Osmangazi University, Turkiye, 2007.

[10] S. K. Meredith, M. Kosseifi, and J. Pastore, ‘Airflow Baffle for Commercial Truck Fuel Efficiency Improvements’, U.S. Patent Appl. 13/715,004, 2014.

[11] V. Modi, S. S. Hill, and T. Yokomizo, ‘Drag Reduction of Trucks Through Boundary-Layer Control’, Journal of Wind Engineering and Industrial Aerodynamics, vol. 54, pp. 583-594, 1995.

[12] P. Gilliéron, and A. Kourta, ‘Aerodynamic Drag Reduction by Vertical Splitter Plates’, Experiments in Fluids, vol. 48, no. 1, pp. 1-16, 2010.

[13] G. Fourrié, L. Keirsbulck, L. Labraga, and P. Gilliéron, ‘Bluff-Body Drag Reduction Using a Deflector’, Experiments in Fluids, vol. 50, pp. 385-395, 2011.

[14] B. Ying, ‘Boundary-layer Control of Bluff Bodies with Application to Drag Reduction of Tractor-trailer Truck Configurations," Master Thesis, University of British Columbia, Canada, 1991.

[15] A. S. Hamdan, ‘Experimental Investigation on Static and Spinning Cylinder and Its Positioning as a Drag Reducer on Truck’s Container’, Bachelor Thesis, Universiti Putra Malaysia, Malaysia, 2022.

[16] H. M. Ali, A. S. M. Rafie, and S. A. M. Ali, ‘Numerical Analysis of Leading Edge Cylinder Aerofoil on Selig S1223 for Moving Surface Boundary Control’, Journal of Aeronautics, Astronautics and Aviation, vol. 53, no. 2, pp. 143-154, 2021.

[17] H. M. Ali, A. S. M. Rafie, S. A. M. Ali, and E. Gires, ‘Computational Analysis of the Rotating Cylinder Embedment onto Flat Plate’, CFD Letters, vol. 13, no. 12, pp. 133-149, 2021.

[18] H. M. Ali, A. S. M. Rafie, M. F. A. Hamid, and S. A. M. Ali, ‘Comparative Computational Study of Double Rotating Cylinder Embedded on Selig S1223 Aerofoil and Flat Plate for High Altitude Platform’, Pertanika Journal of Science and Technology, vol. 30, no. 4, pp. 2767-2788, 2022.

[19] M. Arafat, I. A. Ishak, and A. F. Mohammad, ‘Influence of Mesh Refinement on the Accuracy of Numerical Result for the Next-Generation High-Speed Train Aerodynamics’, OSF Preprints, 2023.

[20] N. Fatchurrohman, and S. Chia, ‘Performance of Hybrid Nano-Micro Reinforced Mg Metal Matrix Composites Brake Calliper: Simulation Approach’, IOP Conference Series: Materials Science and Engineering, vol. 257, 012060, 2017.

[21] B. E. Launder, and D. B. Spalding, ‘The Numerical Computation of Turbulent Flows’, Computer Methods in Applied Mechanics and Engineering, vol. 3, pp. 269-289, 1974.

[22] P. Spalart, and S. Allmaras, ‘A One-Equation Turbulence Model for Aerodynamic Flows’, 30th Aerospace Sciences Meeting and Exhibit, Reno, USA, 6-9 January, 1992.

[23] N. Moradian, D. S. Ting, and S. Cheng, ‘Advancing Drag Crisis of a Sphere via the Manipulation of Integral Length Scale’, Wind and Structures, vol. 14, no. 1, p. 35, 2011.

[24] J. M. Cimbala, and Y. A. Cengel, ‘Fluid Mechanics: Fundamentals and Applications’, McGraw-Hill, 2006.

eISSN 3009-0520
9 773009 052004